ГЕОФИЗИКА И ГЕОЛОГИЯ

UDK 550.384

RECENT DEVELOPMENTS ON PROCESSING AND INTERPRETATION ASPECTS OF FIRST-ORDER REVERSAL CURVES (FORC)

R. Egli, M. Winklhofer

Abstract

Several recent developments in paleo- and environmental magnetism have been based on measurement of first-order reversal curves (FORC). Most notable examples are related to the detection of fossil magnetosomes produced by magnetotactic bacteria and to absolute paleointensity estimates for temperature-sensitive samples, such as meteorites. Future developments in these scientific disciplines rely on improved characterization of natural magnetic mineral assemblages. Promising results have been obtained in several cases with the parallel development of FORC processing protocols on the one hand, and models for idealized magnetic systems on the other hand. Until now, FORC diagrams have been used mainly as a qualitative tool for the identification of magnetic domain state fingerprints, with missing quantitative links to other magnetic parameters. This article bridges FORC measurements and conventional hysteresis parameters on the basis of three types of FORC-related magnetizations and corresponding coercivity distributions. One of them is the well-known saturation remanence, with corresponding coercivity distribution derived from backfield demagnetization data in zero-field FORC measurements. The other two magnetization types are related to irreversible processes occurring along hysteresis branches and to the inversion symmetry of magnetic states in isolated particles, respectively. All together, these magnetizations provide precise information about magnetization processes in single-domain, pseudo-single-domain, and multidomain particles. Unlike hysteresis parameters used in the so-called Day diagram, these magnetizations are unaffected by reversible processes (e.g. superparamagnetism), and therefore well suited for reliable characterization of remanent magnetization carriers. The software package VARIFORC has been developed with the purpose of performing detailed FORC analyses and calculate the three types of coercivity distributions described above. Key examples of such analyses are presented in this article, and are available for download along with the VARIFORC package.

Keywords: rock magnetism, paleomagnetism, environmental magnetism, magnetic mineral characterization, magnetic hysteresis, first-order reversal curves, magnetofossils, magnetic domain states.

Introduction

Several measurement protocols have been developed over the last ~50 years for understanding complex magnetization processes related to technological applications [1, 2], the origin and stability of rock magnetizations [3, 4], and environment-sensitive magnetic minerals in sediments [5, 6]. First-order reversal curves (FORC) provide one of the most advanced protocols for probing hysteresis processes and represent them in a two-dimensional parameter space (i.e. coercivity field H_c and bias

field H_b). The interpretation of hysteresis has evolved from mathematical formalisms based on the superposition of elemental source contributions, called hysterons [7–10], toward physical models of specific magnetic systems, such as non-interacting [11, 12] and interacting [13–17] single-domain (SD) particles, pseudo-single-domain (PSD) particles [18–20], multidomain (MD) crystals [21, 22], and spin glasses [23]. These models provide prototype signatures for specific magnetization processes (e.g. switching, vortex nucleation, domain wall pinning) which can be recognized in FORC diagrams of geologic samples [24, 25]. Some of these signatures occur within a limited subset of FORC space, as for instance along $H_c \approx 0$ (viscosity and MD processes) or along $H_b \approx 0$ (weakly interacting SD particles). Therefore, it is possible to identify the corresponding sources in FORC diagrams of samples containing complex magnetic mineral mixtures [e.g. 26], and, in some cases, to estimate the abundance of magnetic particles associated with these processes [27–30]. Up to the few examples mentioned above, FORC diagrams of geologic materials are mostly interpreted in a qualitative manner. Furthermore, only loose connections have been established with more common magnetic parameters, such as isothermal and anhysteretic remanent magnetizations and domain state-sensitive ratios, although some of these parameters can be directly derived from FORC subsets [e.g. 10, 31, 12].

Quantitative interpretation of FORC measurements is based on the calculation of magnetic parameters associated with specific magnetization processes. Some of these processes produce FORC signatures that are representable only in terms of non-regular functions, whose appearance in the FORC diagram depends strongly on data processing. A meanwhile well-known example of non-regular FORC signatures is represented by the so-called central ridge produced by non-interacting SD particles [12, 29]. Magnetic viscosity is another example associated with a vertical ridge near $H_c = 0$ [32]. On the other hand, most magnetic processes in weakly magnetic natural samples produce continuous FORC contributions with very low amplitudes, which are below the significance threshold attainable with conventional FORC processing [29]. Since the introduction of FORC measurements to rock magnetism [15, 24], some studies have been dedicated to selected aspects of FORC processing, such as computational optimization [33], locally weighted regression [34], error calculation [35], and variable polynomial regression smoothing [29]. These improvements have been merged into a single FORC processing procedure called VARIFORC (VARIable FORC smoothing) [29]. The principal advantage of VARIFORC consists in the possibility of processing FORC data containing high-amplitude, non-regular FORC signatures as well as low-amplitude, continuous backgrounds, using a local compromise between high resolution and noise suppression requirements. First applications of this technique enabled full characterization of SD signatures in pelagic carbonates [30].

Meanwhile, VARIFORC has been complemented with routines for the automatic separation of different FORC contributions, and the calculation of corresponding magnetizations and coercivity distributions. The full VARIFORC package, including a detailed user manual, is available at http://www.conrad-observatory.at/cmsjoomla/en/download. VARIFORC runs on Wofram Mathematica® and Wofram Player Pro® (http://store.wolfram.com/catalog, Player Pro license: 195 €). Application examples of quantitative FORC analysis performed with VARIFORC are discussed in this paper.

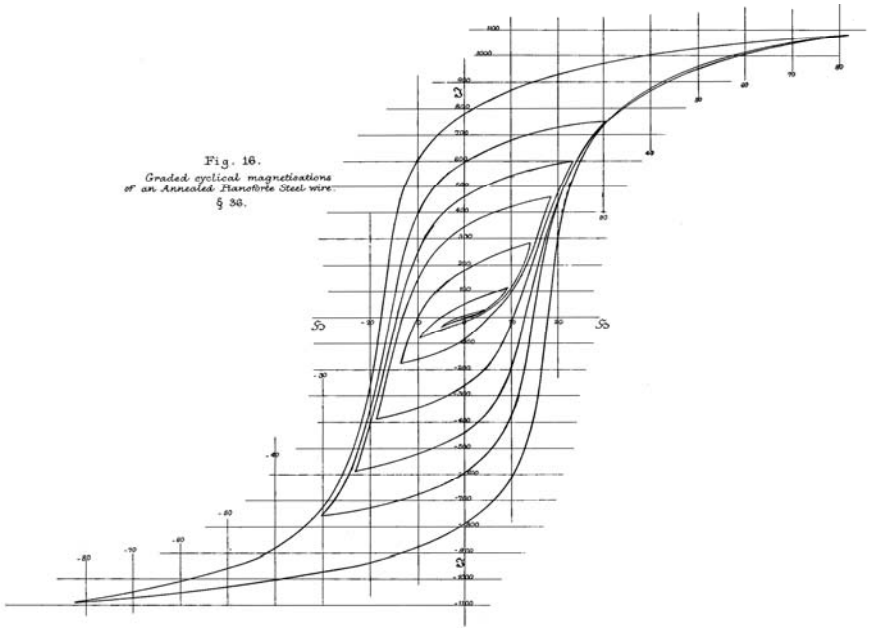

Fig. 1. Original figure from *Ewing* [36] showing the hysteresis measurement of a piano wire (see the IRM Quarterly Vol. 22 for a story about Sir Alfred Ewing's first hysteresis measurements). The measurement shown here represents an AF demagnetization curve, as a possible method for accessing the inner area of hysteresis loops

1. A brief introduction to FORC diagrams

1.1. Reversible and irreversible hysteresis processes. Ferrimagnetic materials are characterized by complex magnetic properties that depend on their past magnetic and thermal history. Memory of previously applied fields gives rise to the well-known phenomenon of magnetic hysteresis. The discovery of magnetic hysteresis is credited to Sir Alfred James Ewing (1855–1955), who measured the first hysteresis loop (Fig. 1) on a piano wire [36]. While the main characteristics of a hysteresis loop are summarized by four magnetic parameters yielding the well known Day diagram [37–39], much more detailed information on magnetization processes can be obtained by accessing the inner area of hysteresis loops. This is possible by in-field measuring protocols involving a sequence of field sweep reversals. The oldest example of such sequences is the alternating-field (AF) demagnetization [1], in which the field sweep is reversed at increasingly small field amplitudes, until a demagnetized, so-called anhysteretic state $H = M = 0$ is reached (Fig. 1).

Other measuring protocols for accessing the inner area of a hysteresis loop are possible, and the FORC protocol described by *Pike et al.* [15] is just one of them. All protocols start from a well-defined magnetic state obtained by saturating the sample in a large field. The first magnetization curve obtained by sweeping the magnetic field from positive or negative saturation coincides with one of the two major hysteresis loop branches $M_{\pm}(H)$. Hysteresis branches are also known as a zero-order curves, because they originate directly from a saturated state. If the field sweep producing a zero-order curve is reversed at a reversal field H_{r}, before saturation is

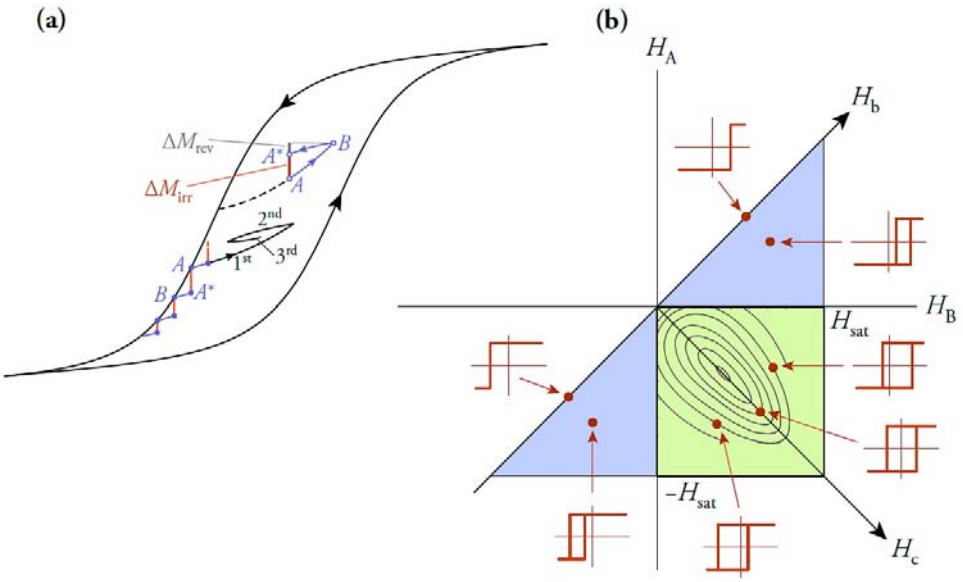

Fig. 2. Preisach theory in a nutshell. (a) The major hysteresis loop (black lines with large arrows) is composed of two zero-order magnetization curves starting from positive and negative saturation, respectively. First-order magnetization curves originate from the major hysteresis if the field sweep is reversed (black curve labeled with 1st). Higher-order magnetization curves (curves labeled with 2nd and 3rd) are obtained after successive field sweep reversals. Any point inside the major hysteresis loop can be accessed by first-order magnetization curves (dashed black line). For any of these points (e.g. point *A* at the end of the dashed line), magnetization changes can be decomposed into a reversible (ΔM_{rev}) and an irreversible (ΔM_{irr}) component by sweeping the field a little further to point *B* and then back to the original field, ending with point *A**, which, because of ΔM_{irr}, does not coincide with *A*. The initial parts of first-order curves originating from the upper hysteresis branch (blue segments) define the irreversible component (red bars) of magnetization changes along this branch. (b) The Preisach diagram is a representation of hysteresis processes as the sum of elemental contributions from rectangular hysteresis loops (hysterons, sketched in red) with switching fields H_A and H_B. Because $H_B \geq H_A$ by definition, hysteron coordinates (H_A, H_B) plot below the $H_A = H_B$ diagonal, over a triangular area (colored) limited by the saturation field H_{sat} above which magnetic hysteresis is fully reversible. Further distinctions can be made between (1) closed hysterons with $H_A = H_B$, (2) hysterons with only one possible state in zero field (positive or negative saturation, blue areas), and (3) hysterons with two possible states in zero field (so-called magnetic remanence carriers, green square). The Preisach space can also be expressed in transformed coordinates representing coercivity (i.e. hysteron openings $H_C = (H_B - H_A)/2$) and the bias field (i.e. hysteron horizontal shifts $H_b = (H_B + H_A)/2$). Hysteron examples (red) are given for selected points of the Preisach space, which can be understood as samples of the Preisach distribution. Contour lines over the region occupied by remanence-carrying hysterons (green) represent a Preisach distribution obtained for interacting SD particles by *Dunlop et al.* [69]. In the Preisach–Néel model, H_c- and H_b-coordinates coincide with coercivities and interaction fields of real SD particles, respectively

reached, a new magnetization curve $M(H_r, H)$ originates from the major hysteresis loop (Fig. 2a). This curve represents a first-order magnetization, also known as first-order reversal curve in case of FORC measurements. A set of first-order curves branching from the major hysteresis loop at different reversal fields covers the entire area enclosed by the loop, accessing a much larger number of magnetization states that cannot be obtained with simple hysteresis measurements. If the field sweep is

reversed again while a first-order curve is measured, a second-order curve is obtained, and so on. Within this context, AF demagnetization is a sequence of nested magnetization curves with increasing order.

When describing magnetization curves, an important distinction is made between magnetization changes due to reversible and irreversible processes. The two types of processes occurring along any magnetization curve are discriminated by comparing a small portion $M_A \to M_B$ of the curve between close fields H_A and H_B with the magnetization M_A^* obtained by sweeping the field from H_B back to H_A (Fig. 2a). Hysteresis, known in this context as magnetic memory, ensures that $M_B \to M_A^*$ does not follow the same path as $M_A \to M_B$, in which case $M_A^* \neq M_A$ [8]. The difference $M_A^* - M_A$ is the irreversible magnetization change occurring when sweeping the field from H_A to H_B, while $M_B - M_A^*$ is the reversible change. The sum of the two contributions gives $M_B - M_A$, as expected.

1.2. Preisach diagrams. Because *n*-th order magnetization curves depend on $n+1$ parameters (i.e. *n* reversal fields and one measuring field), interpretation of first- and higher-order curves requires a parameter space model. The best known bivariate hysteresis model has been implemented by *Preisach* [7] for the characterization of transformer steel. The Preisach model assumes that magnetization curves are the result of magnetic switching in elemental rectangular hysteresis loops (so-called hysterons). Hysterons are characterized by two switching fields $H_\mathrm{A} \le H_\mathrm{B}$ where the magnetization jumps discontinuously from the lower to the upper branch and vice versa (Fig. 2b). Each hysteron is thus represented by a point in $(H_\mathrm{A}, H_\mathrm{B})$-space, and macroscopic magnetic volumes or magnetic particle assemblages are described by a bivariate statistical distribution $P(H_\mathrm{A}, H_\mathrm{B})$ of hysteron switching fields, known as the Preisach distribution.

Hysterons are merely a mathematical construct and do generally not correspond to discrete particles or sample volumes. Nevertheless, the bivariate Preisach distribution provides intrinsically more information than any one-dimensional magnetization curve. The simplest physical interpretation of a Preisach distribution has been proposed by *Néel* [40] with what is known as the Preisach–Néel model of single-domain (SD) particles. This model relies on the resemblance between hysteresis loops of individual SD particles with uniaxial anisotropy [41] on the one hand, and symmetric Preisach hysterons (i.e. $H_\mathrm{A} = -H_\mathrm{B}$) on the other hand. Both are characterized by only two magnetization states (one for each hysteresis branch) with discontinuous transitions at $H_\mathrm{A} = -H_\mathrm{c}$ and $H_\mathrm{B} = +H_\mathrm{c}$. The Preisach distribution of isolated SD particles is thus concentrated along the $H_\mathrm{A} = -H_\mathrm{B}$ diagonal of the Preisach space and coincides with the well-known coercivity or switching field distribution.

In interacting SD particle assemblages, magnetic switching of individual particles occurs in a total field given by the sum of the applied field and an internal, so-called interaction field H_b, which is the sum of dipole fields produced by the magnetic

moments of the other particles. Whenever $H_b \neq 0$, elemental hysteresis loops are shifted horizontally, so that magnetic switching occurs at $H_A = H_b - H_c$ and $H_B = H_b + H_c$. Because the interaction field is a local variable determined by the spatial arrangement and magnetization of neighbor particles, the Preisach distribution of interacting SD particles can be represented as the product of a coercivity distribution $f(H_c)$ and an interaction field distribution $g(H_b)$:

$$P = f(H_c)g(H_b) \tag{1}$$

with $H_c = (H_B - H_A)/2$ and $H_b = (H_B + H_A)/2$ (Fig. 2b). More generally, H_c and H_b are known as the coercivity field and the bias field of hysterons. The appealing simplicity of the Preisach–Néel model has promoted the use of the transformed coordinates (H_c, H_b) (whereby H_b is also called H_u or H_i), instead of the original Preisach fields H_A and H_B.

The Preisach space spanned by hysteresis processes that are saturated in fields $|H| < H_{sat}$ is a triangular region delimited by the diagonal line $H_B \geq H_A$ (by definition of hysteron switching fields), and by $H_A > -H_{sat}$, $H_B < +H_{sat}$, respectively (Fig. 2b). This space can be further subdivided into a square region with $H_A < 0$ and $H_B > 0$ where hysterons can have two magnetization states in zero field, and the remaining space where hysterons are negatively or positively saturated when no external fields are applied. The square region is particularly relevant to paleo- and rock magnetism, because remanent magnetizations originate only from hysterons located within it. In particular, the saturation remanent magnetization M_{rs} corresponds to the integral of the Preisach function over this region, i.e.

$$M_{rs} = \int_{H_A=-H_{sat}}^{0} \int_{H_B=0}^{+H_{sat}} P(H_A, H_B)\, \mathrm{d}H_A \mathrm{d}H_B. \tag{2}$$

On the other hand, the saturation magnetization M_s corresponds to the integral of the Preisach function over the entire domain defined by $H_B \geq H_A$.

1.3. The FORC distribution. Several measurement protocols have been developed in order to obtain experimental Preisach function estimates. What is nowadays known as the FORC protocol has been first described by *Hejda and Zelinka* [9]. With this protocol, first-order magnetization curves $M(H_r, H)$ measured upon positive sweeps of H (i.e. H increases) from reversal fields H_r, define the so-called FORC function

$$\rho(H_r, H) = -\frac{1}{2}\frac{\partial^2 M}{\partial H_r \partial H} \tag{3}$$

[42]. This function coincides with the Preisach distribution in case of measurements performed on samples that are correctly described by the Preisach model. Because real samples rarely satisfy this condition, empirical distributions such as Eq. (3) do generally not coincide with the Preisach distribution up to few exceptions [e.g. 43].

For example, the Preisach distribution is a strictly positive probability function, while FORC diagrams can have negative amplitudes [11]. Several modifications of the original Preisach model have been developed in order to account for such differences. The so-called moving Preisach models [44] take into account the effect of macroscopic magnetization states on the intrinsic hysteron properties, and are used for instance to describe magnetization-dependent interaction fields. Magnetic viscosity, on the other hand, is accounted by Preisach models with stochastic inputs simulating thermal fluctuations of switching fields [45, 46].

Modifications of the Preisach formalism are not sufficient to explain all aspects of FORC functions, especially in case of non-SD magnetic systems. Therefore, physical FORC models have been developed in order to properly interpret magnetic processes in isolated [11] and interacting [16, 17] SD particles, nucleation of magnetic vortices in PSD particles [19, 47], domain wall displacement in MD crystals [21, 22], and magnetic viscosity [32]. Magnetic models of idealized systems yield characteristic signatures of the FORC function that can be used as fingerprints for the identification of magnetic minerals in geologic samples [24]. In some cases, theses signatures are precisely determined to the point that quantitative analysis is possible [12, 30, 31].

The remaining part of this section is dedicated to the implementation of a general FORC model that will be used to interpret the properties of SD, PSD, and MD samples presented in this article. For this purpose, a relatively simple magnetic system with few magnetization states is considered. This system corresponds to the micromagnetic hysteresis simulation of a cluster of seven strongly interacting SD particles (Fig. 3).

This system corresponds to the micromagnetic simulation of a cluster of seven strongly interacting SD particles. The upper branch of the major hysteresis loop contains three magnetization jumps produced by abrupt transitions between four magnetic states with magnetizations M_0, M_1, M_2, and M_3. These states represent continuous segments of the upper hysteresis branch. If the field sweep is reversed within the positively saturated state M_0, the resulting first-order magnetization curves will always coincide with M_0. Because these curves are identical, $\partial M/\partial H_\mathrm{r} = 0$ and no contribution to the FORC function is obtained. If the reversal field is decreased below the first magnetization jump at $H_{\mathrm{r},1}$, first-order curves will start from M_1 instead of M_0, and continue along M_1 until a magnetization jump (labeled with '*1,1*' in Fig. 3a) will bring the magnetization M_1 back to positive saturation (i.e. M_0). The finite difference between the last first-order curve coinciding with M_0 and the first one starting coinciding with M_1 creates a contribution

$$\rho = \frac{1}{2}\delta(H_\mathrm{r} - H_{\mathrm{r},1})\frac{\partial}{\partial H}(M_1 - M_0) \tag{4}$$

to the FORC distribution, where $\delta(H_\mathrm{r} - H_{\mathrm{r},1})$ is the Dirac impulse function accounting for the magnetization jump at $H_{\mathrm{r},1}$. Because $\delta(H_\mathrm{r} - H_{\mathrm{r},1})$ is zero everywhere, except for $H_\mathrm{r} - H_{\mathrm{r},1} = 0$, Eq. (4) produces a diagonal ridge in FORC space (Fig. 3b). Using

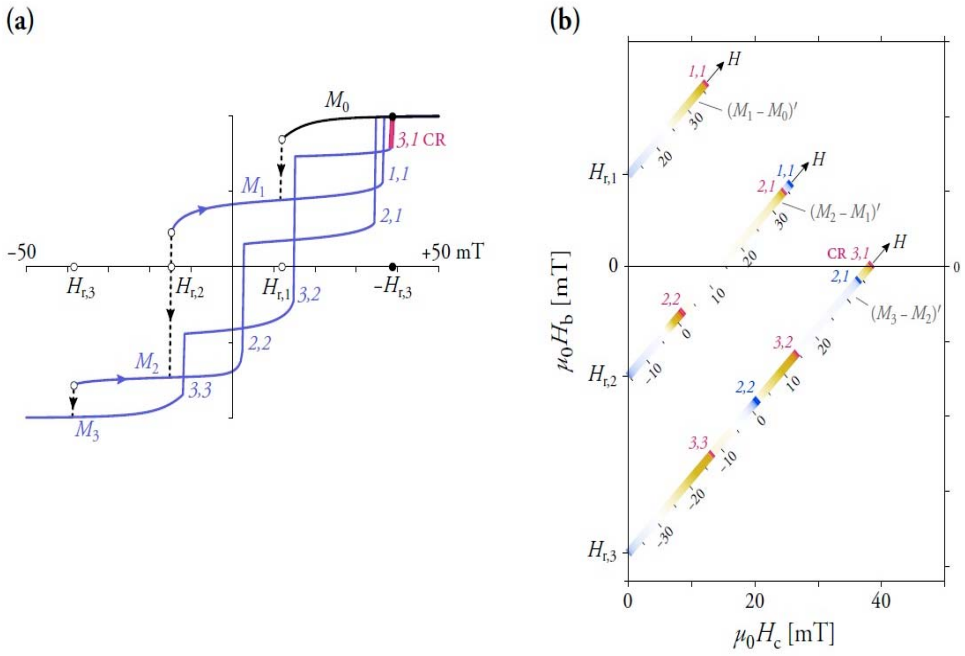

Fig. 3. FORC model of a linear chain of 7 SD magnetite particles with elongation $e = 1.3$ and long axes perpendicular to the chain axis. This model represents the simulation of a collapsed magnetosome chain according to Fig. 9a in *Shcherbakov et al.* [48]. In this example, the chain axis forms an angle of 75° with the applied field direction. Magnetization jumps along the upper branch of the major hysteresis loop are indicated by dashed lines. Cursive number pairs are used to count discontinuities of first-order curves M_1, M_2, and M_3 (blue lines). For example, (*2,2*) is the second jump (counted from the right) occurring along M_2. Any measurable FORC coincides with M_0, M_1, M_2, or M_3. The amplitude of the last magnetization jump on M_3 (magenta) defines the contribution M_{cr} of the central ridge to the FORC diagram shown in (b). (b) FORC diagram calculated from (a), consisting of three diagonal ridges defined by first derivatives $(M_i - M_{i-1})'$ of differences between M_0, M_1, M_2, and M_3. The ridges width is exaggerated in order to show the color coding for positive (orange to magenta) and negative (blue) contributions. Cursive number pairs indicate peaks of the FORC function produced by magnetization jumps with the same labels as in (a). One of the peaks, labeled with CR, contributes to the central ridge and is generated by the last magnetization jump (i.e. *3,1*) of the last FORC (i.e. M_3). All FORC contributions are enclosed in a triangular region defined by vertices with coordinates $(0, \pm H_{sat})$ and $(H_{sat}, 0)$, where $H_{sat} \approx 40$ mT is the field above which hysteresis becomes fully reversible

the coordinate transformations $H_c = (H - H_r)/2$ and $H_b = (H + H_r)/2$, the ridge location is given by a line with equation $H_b = H_{r,1} + H_c$. FORC contributions along this line are proportional to the derivative of $M_1 - M_0$ and are of two fundamental types. The first type occurs at points where M_0 and M_1 are continuous, and is proportional to differences between their slopes. Such FORC contributions are magnetically reversible, because a small change of the applied field H does not nucleate magnetic state transitions. On the other hand, magnetically irreversible contributions occur at magnetization jumps occurring along M_1 (e.g. jump '*1,1*' in Fig. 3b). In this case, the derivative of $M_1 - M_0$ is a Dirac impulse with amplitude $\Delta M_{1,1}$, contributing with a point peak

$$\rho = \frac{1}{2}\Delta M_{1,1}\delta(H_{\mathrm{r}} - H_{\mathrm{r},1})\delta(H - H_{1,1}) \tag{5}$$

to the FORC distribution. Eqs. (4)–(5) can be generalized to any pair of first-order curves, giving rise to as many diagonal ridges in FORC space, as discrete magnetization jumps are encountered along the upper hysteresis branch. The FORC function is thus fully described by the sum of all diagonal ridges, i.e.

$$\rho = \frac{1}{2}\sum_{i=1}^{n}\delta(H_{\mathrm{r}} - H_{\mathrm{r},i})\frac{\partial}{\partial H}(M_i - M_{i-1}) \tag{6}$$

An important characteristics of this FORC model is that both reversible and irreversible contributions can have positive and negative amplitudes, depending on the slopes of first-order curves, and on whether a magnetization jump occurs along M_i or M_{i-1}.

The FORC function of a simple system with few magnetization states, such as in the example of Fig. 3, is given by a certain number of infinite, isolated peaks corresponding to discrete transitions between magnetic states. Each peak is preceded by a sort of diagonal "shadow" produced by the pronounced curvature of magnetization curves in proximity of magnetic state transitions. Peak positions define so-called switching or nucleation fields in which magnetic state transitions occur. Small modifications of the magnetic system, as for instance the introduction of an additional particle in the SD cluster model of Fig. 3, modify critical fields and eventually produce additional magnetization states with corresponding transitions. Therefore, samples containing large numbers of heterogeneous magnetic particles generate a dense "cloud" of peaks merging into a continuous FORC distribution. Because individual peaks can be positive or negative, some regions of the FORC diagram might be characterized by negative amplitudes. In general, all FORC contributions are contained within a triangular region defined by vertices with coordinates $(0,\pm H_{\mathrm{sat}})$ and $(H_{\mathrm{sat}},0)$.

An important characteristic of the general FORC model described above is related to the inversion symmetry of magnetic states. This symmetry ensures that the last magnetization jump on the upper branch (i.e. the transition from M_2 to M_3 in Fig. 3a) is always accompanied by an identical jump on the following first-order curve, which coincides with the lower hysteresis branch (i.e. jump '*3,1*' in Fig. 3a). This jump produces an infinite peak on the last diagonal ridge of the FORC diagram (Fig. 3b), which is located exactly on $H_{\mathrm{b}} = 0$. This is because the last diagonal stripe starts at a certain negative reversal field $H_{\mathrm{r,last}}$ and ends with a jump occurring at $H = -H_{\mathrm{r,last}}$, so that $H_{\mathrm{b}} = H_{\mathrm{r,last}} - H_{\mathrm{r,last}} = 0$. While other peaks can occur everywhere in FORC space, the peak associated with $H_{\mathrm{r,last}}$ is always placed exactly at $H_{\mathrm{b}} = 0$. A sample containing many isolated (i.e. non-interacting) particles with few magnetic states will produce a corresponding number of FORC peaks along $H_{\mathrm{b}} = 0$, while other peaks contribute to a distributed background. The superposition of all peaks with $H_{\mathrm{b}} = 0$ appears as an infinitely sharp, so-called central ridge [12]. Its existence has been first predicted for non-interacting uniaxial SD particles [11], which

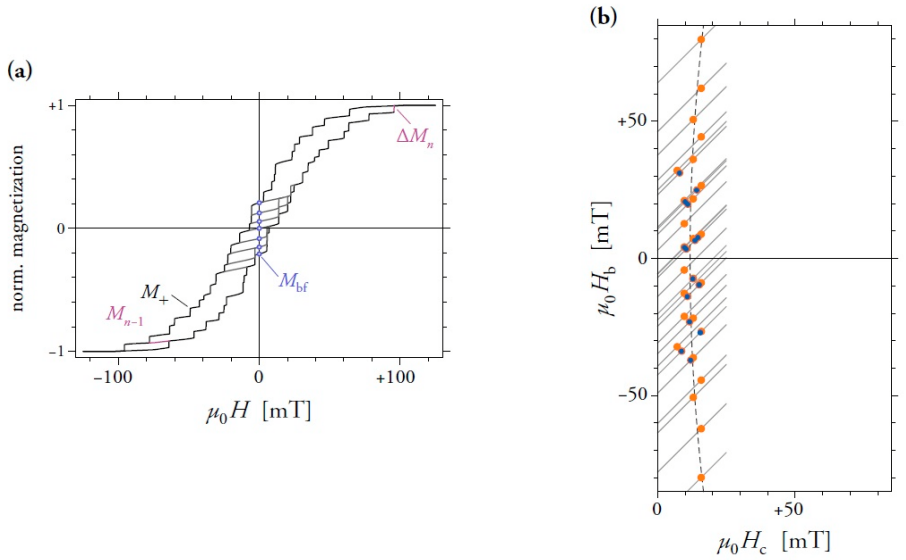

Fig. 4. (a) Model hysteresis loop (black) and FORCs (gray) generated by three MD particles with demagnetizing factors of 0.1, 0.2, and 0.3, respectively, calculated according to *Pike et al.* [21]. Only FORCs necessary for measurement of the backfield demagnetization curve M_{bf} (blue dots) are shown for clarity. The last FORC M_{n-1} that does not coincide with the lower hysteresis branch is show in purple. It merges with the lower hysteresis branch before the last magnetization jump ΔM_n has occurred, so that no central ridge contributions are produced. (b) FORC diagram corresponding to the MD hysteresis model shown in (a). Gray diagonal lines are individual FORC trajectories along which irreversible magnetization processes are recorded as positive (orange dots) and negative (blue dots) peaks. The dashed line is a quadratic fit to the dots showing clustering around the crest of a 'crescent-shaped' distribution as discussed in *Church et al.* [22]

represent the simplest possible case of particles with two magnetic states, and observed in a magnetofossil-bearing lake sediment [12]. Because of the theoretically infinite sharpness of the central ridge, high-resolution FORC measurements and proper processing are necessary for its identification. Since its first observation, the central ridge has been found to be a widespread signature of freshwater and marine sediments containing magnetofossils [26]. Two conditions must be met for the existence of a central ridge: first, magnetic particles should not interact with each other, since the presence of an interaction field destroys the inversion symmetry of single particle hysteresis loops by shifting them horizontally. Second, individual particles should have only few magnetization states, so that the lower hysteresis branch merges directly with the upper branch, without joining any other first-order curve. For example, MD particles with many domain wall pinning sites produce a large number of individual FORC peaks, none of which must forcedly occur at $H_b = 0$ (Fig. 4).

In any case, the central ridge is not an exclusive feature of SD particles, as it can occur in any collection of non-interacting particles with few magnetization states (e.g. PSD). Some examples will be provided with the discussion of PSD magnetization processes in Section 3.2.

2. Coercivity distributions derived from FORC measurements

FORC measurements subsets define three types of coercivity distributions that provide a bridge with conventional parameters used in rock magnetism since several decades. These coercivity distributions originate from three particular FORC segments (Fig. 5): (1) the initial part $M(H_r, H \to H_r)$ of each curve and its departure from the upper hysteresis branch, (2) the remanent magnetization $M(H_r, 0)$ of each curve, and (3) the point $H = -H_r$ of each curve where the applied field equals the reversal field amplitude. These regions define magnetization curves that will be discussed in the following.

2.1. Backfield coercivity distribution. Backfield or DC demagnetization of a positively saturated sample is obtained by measuring its remanent magnetization after application of increasingly large negative fields [50]. The applied negative fields are equivalent to reversal fields H_r of the FORC protocol (Fig. 6), so that the backfield demagnetization curve is given by FORC remanent magnetizations $M(H_r, 0)$. The corresponding backfield coercivity distribution is defined as the first derivative of $M(H_r, 0)$, i.e.

$$f_{bf}(x) = -\frac{1}{2}\frac{dM(-x,0)}{dx}. \tag{7}$$

The backfield coercivity distribution can be determined very precisely with the same polynomial regression method used to calculate FORC diagrams. The factor 1/2 in Eq. (7) ensures that the integral of f_{bf} over all fields yields the saturation remanence M_{rs} of the sample. Moreover, f_{bf} is defined only for positive arguments, which correspond to negative reversal fields, because the remanent magnetization of curves starting at $H_r > 0$ cannot be measured. Within the Preisach model, the argument of f_{bf} coincides with the coercivity field H_c of hysterons, and $f_{bf}(H_c)dH_c$ coincides with the M_{rs}-contribution of all hysterons with coercivities comprised between H_c and $H_c + dH_c$.

2.2. Reversal coercivity distribution. Initial FORC slopes can be used to calculate irreversible magnetization changes

$$\Delta M_{irr} = M(H_r + \delta H, H_r + \delta H) - M(H_r, H_r + \delta H) \tag{8}$$

along the upper hysteresis branch (Fig. 7), where δH is the (constant) field increment used for the measurements. The sum of all ΔM_{irr}'s obtained from consecutive FORCs starting at reversal fields $H_r \le x$ defines a magnetization curve $M_{irr}(x)$ with the following meaning: if reversible magnetization processes are removed from the upper hysteresis branch, the resulting 'irreversible hysteresis' branch would coincide with M_{irr} up to a constant (Fig. 7b). The so-called reversal coercivity distribution is defined by analogy with backfield demagnetization as

$$f_{irr}(x) = -\frac{1}{2}\frac{dM_{irr}(-x)}{dx} = -\frac{1}{2}\frac{\partial M(H_r, H)}{\partial H_r}\bigg|_{H_r = H = -x} \tag{9}$$

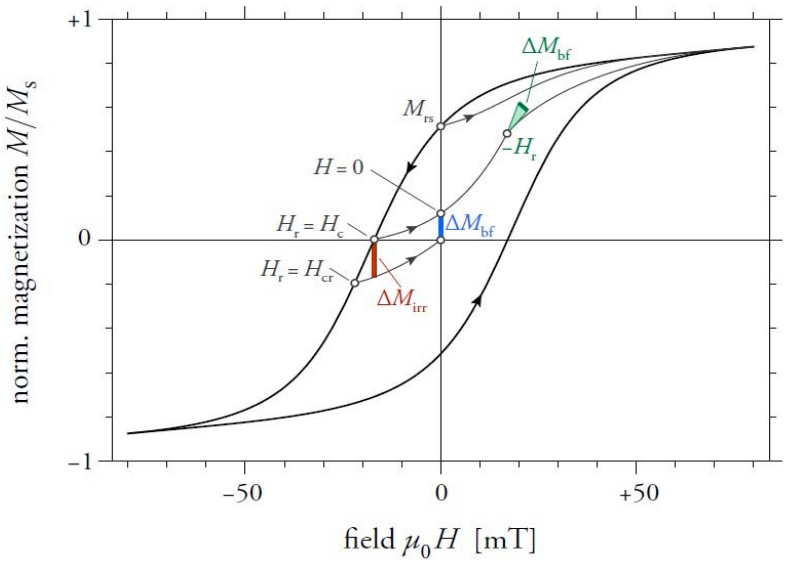

Fig. 5. Relevant magnetization processes captured by FORCs. ΔM_{irr} (red bar) is the irreversible magnetization change along the upper hysteresis branch, defined by the initial difference between FORCs originating at consecutive reversal fields H_r. In this example, H_r-values have been chosen to coincide with the coercivity H_c and the coercivity of remanence H_{cr} for didactic purposes. The difference between the same two FORCs in zero field ($H = 0$, blue bar) defines a contribution ΔM_{bf} to the backfield demagnetization curve. Finally, the abrupt slope change of FORCs at $H = H_r$ defines the contribution ΔM_{cr} (green) to the central ridge. The FORC starting at $H_r = 0$, where $M = M_{rs}$, is called saturation initial curve [49]. In ensembles of non-interacting SD particles, this curve coincides with the upper hysteresis branch because negative fields are required to switch them from positive saturation

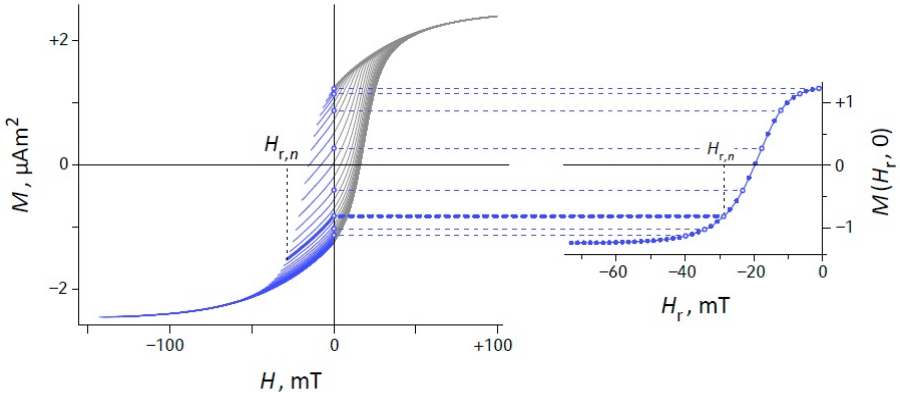

Fig. 6. Construction of a backfield demagnetization curve (right) from FORC measurements (left) of a magnetofossil-bearing pelagic carbonate. FORC portions that are actually swept during backfield measurements are shown in blue, and some zero-field measurements are highlighted with blue circles. Remanent magnetization measurements $M_r = M(H_r, 0)$ on FORCs beginning at $-H_r$ define the backfield curve coordinates (H_r, M_r)

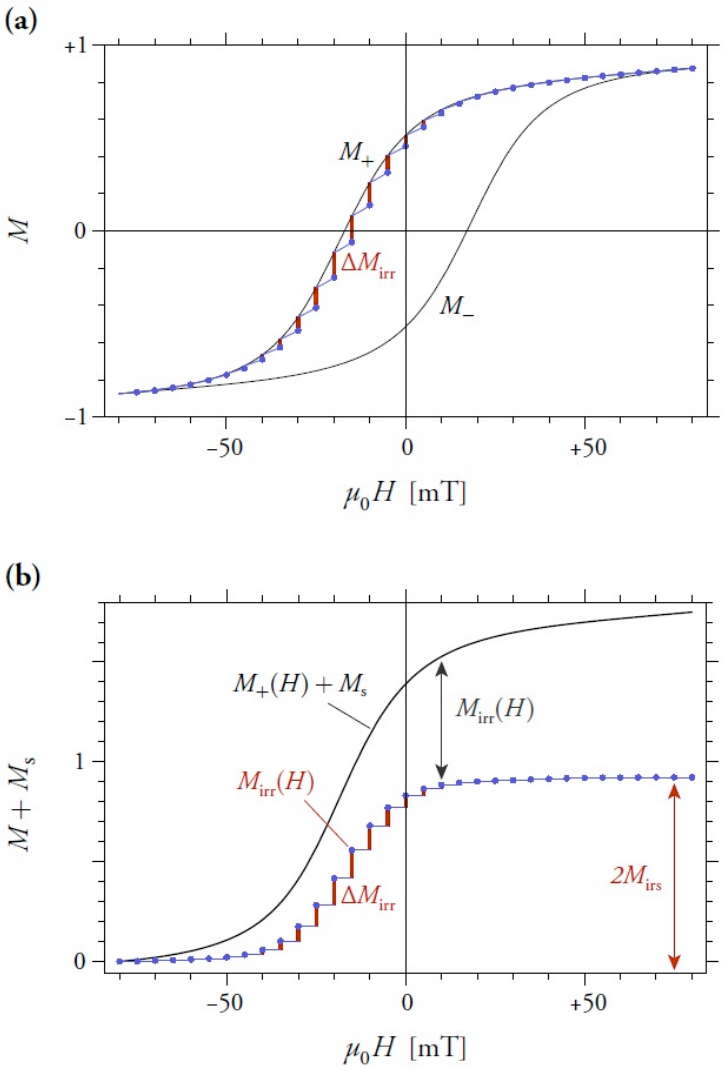

Fig. 7. Construction of the magnetization curve corresponding to irreversible processes along the upper hysteresis branch. (a) Irreversible magnetization changes ΔM_{irr} (red) defined by the initial parts of all FORCs (blue). (b) Upper hysteresis branch M_{+} (black curve) after adding the saturation magnetization M_{s}, and irreversible magnetization curve $M_{\mathrm{irr}}(H)$ reconstructed by integrating all magnetization steps ΔM_{irr} shown in (a). The saturation value $M_{\mathrm{irr}}(H \to \infty)$ is the total irreversible magnetization $2M_{\mathrm{irs}}$ of the hysteresis branch

The factor 1/2 in Eq. (9) has been introduced to ensure that the total integral M_{irs} of f_{irr} is a magnetization with the following properties: $0 < M_{\mathrm{irs}} \le M_{\mathrm{s}}$ for any sample, and $M_{\mathrm{irs}} = M_{\mathrm{s}}$ in absence of reversible processes. Unlike M_{rs}, the parameter M_{irs} includes all irreversible processes occurring along the major hysteresis loop and shall therefore be called irreversible saturation magnetization. The saturation value $M_{\mathrm{irr}}(H \to \infty)$ is the total irreversible magnetization $2M_{\mathrm{irs}}$ of the hysteresis branch.

A fundamental property of M_{irs} is that it coincides with the total integral of the FORC function, because, using Eq. (6):

$$\iint\limits_{H_{\mathrm{r}},H} \rho(H_{\mathrm{r}},H)\,\mathrm{d}H_{\mathrm{r}}\,\mathrm{d}H = \frac{1}{2}\sum_{i=1}^{n}(M_{i-1}-M_i)\big|_{H=H_{\mathrm{r},i}} = \frac{1}{2}\sum_{i=1}^{n}\Delta M_i = M_{\mathrm{irs}}. \qquad (10)$$

This important result implies that, while reversible magnetization processes can contribute locally to the FORC function, these local contributions cancel each other out upon integration over the FORC space.

The definitions of f_{bf} and f_{irr} are analogous, since they both rely on differences between consecutive FORCs evaluated at $H=0$ and $H=H_{\mathrm{r}}$, respectively, and are both related to the FORC starting at $H_{\mathrm{r}}=-x$ (Fig. 5). An important difference, on the other hand, is that the argument of f_{irr} can be positive as well as negative, unlike other coercivity distributions. Positive arguments of f_{irr} correspond to measurements of the upper hysteresis branch in negative fields and vice versa. Similarly, positive arguments of f_{bf} correspond to negative fields used for DC demagnetization. Furthermore, $f_{\mathrm{irr}}(0)=f_{\mathrm{bf}}(0)$ by the definitions given with Eq. (7) and Eq. (9).

2.3. Central ridge coercivity distribution. The central ridge coercivity distribution is best explained by considering an isolated magnetic particle with any domain state. A first-order curve starting from the upper hysteresis branch just after a magnetization jump has occurred at $H_{\mathrm{r}}<0$ will contribute to the central ridge if another magnetization jump is encountered at $H=-H_{\mathrm{r}}$ while sweeping the field back towards positive values, before merging with the previous FORC. Usually, magnetization jumps can occur at any field and there is no particular reason for having one exactly at $H=-H_{\mathrm{r}}$. In this case, FORC contributions accumulate at $H_{\mathrm{b}}=0$ as over any other place in FORC space, generating a continuous FORC distribution. An exception is provided by the FORC originating from the upper hysteresis branch just after the last magnetization jump. This curve coincides by definition with the lower hysteresis branch. Because of inversion symmetry, the lower branch will contain a symmetric magnetization jump at $H=-H_{\mathrm{r}}$. If the lower branch merges with the previous FORC curve before $H=-H_{\mathrm{r}}$ is reached, as it is commonly the case for MD hysteresis (Fig. 4a), the jump at $H=-H_{\mathrm{r}}$ will not contribute to the FORC diagram, because the two curves are identical and $\partial M/\partial H_{\mathrm{r}}=0$. Otherwise, there will be a contribution to the central ridge in form of a peak with FORC coordinates $(H_{\mathrm{c}},H_{\mathrm{b}})=(-H_{\mathrm{r}},0)$ (Fig. 3). Because these contributions are placed exactly at $H_{\mathrm{b}}=0$, they produce a ridge of the form

$$\rho_{\mathrm{cr}}(H_{\mathrm{c}},H_{\mathrm{b}}) = \frac{1}{2}f_{\mathrm{cr}}(H_{\mathrm{c}})\delta(H_{\mathrm{b}}) \qquad (11)$$

where f_{cr} is the so-called central ridge coercivity distribution [12]. In FORC diagrams obtained from real measurements, the infinite sharpness of ρ_{cr} is regularized

by replacing the Dirac impulse with an appropriate function of H_b that takes into account the smoothing effects of measurements performed with finite field increments. A rigorous treatment of such effects is given in *Egli* [29]. The central ridge coercivity distribution is obtained from real measurements in two steps: first, the central ridge contribution ρ_{cr} to the FORC diagram is isolated from the continuous background produced by other processes, then ρ_{cr} is integrated over H_b so that

$$f_{cr}(H_c) = \int_{-\infty}^{+\infty} \rho_{cr}(H_c, H_b)\, dH_b. \tag{12}$$

While the amplitude of ρ_{cr} depends on the resolution of FORC measurements and FORC processing, f_{cr} is independent of any measuring and processing parameter and reflects intrinsic magnetic properties. The complex operation of isolating the central ridge and calculating f_{cr} is performed automatically by VARIFORC with few controlling parameters described in the user manual that can be downloaded with the program package.

The total magnetization M_{cr} associated with the central ridge is obtained by integrating f_{cr} over H_c and represents the total contribution of last magnetization jumps in isolated magnetic particles. Accordingly, M_{cr}/M_{irs} is the ratio between the last magnetization jump ΔM_n of a hysteresis branch and the sum of all magnetization jumps over the same branch. In case of non-interacting, uniaxial SD particles, $\Delta M_n = \Delta M_1$ is the only magnetization jump of single particle hysteresis, so that $M_{cr}/M_{irs} = 1$. As soon as additional magnetic states begin to exist in small PSD particles, the relative amplitude of ΔM_n decreases with respect to the sum M_{irs} of all magnetization jumps, and $M_{cr}/M_{irs} < 1$, until $M_{cr} = 0$ is reached in MD-like systems.

3. Examples

The physical meaning of FORC diagrams and derived coercivity distributions is best illustrated with topic examples related to SD, PSD, and MD magnetic particle assemblages. The hysteresis properties of samples discussed in this section are summarized by the Day diagram of Fig. 8.

3.1. SD magnetic assemblages. The first example is a conceptual model of a sample containing a small number of non-interacting, uniaxial SD particles with rectangular (Fig. 9a) and curved (Fig. 9c) single-particle hysteresis. Reversible processes (i.e. magnetic moment rotation in the applied field) are absent in the first case. The SD particles have two stable magnetization states in fields $|H| < H_s$, where H_s is a particle-specific switching field. Transitions from one magnetization state to the other in individual particles once their specific H_s-values have been reached is seen in Fig. 9 as a series of magnetization jumps. These jumps represent irreversible magnetization processes, while reversible magnetic moment rotation (Fig. 9c) occurs

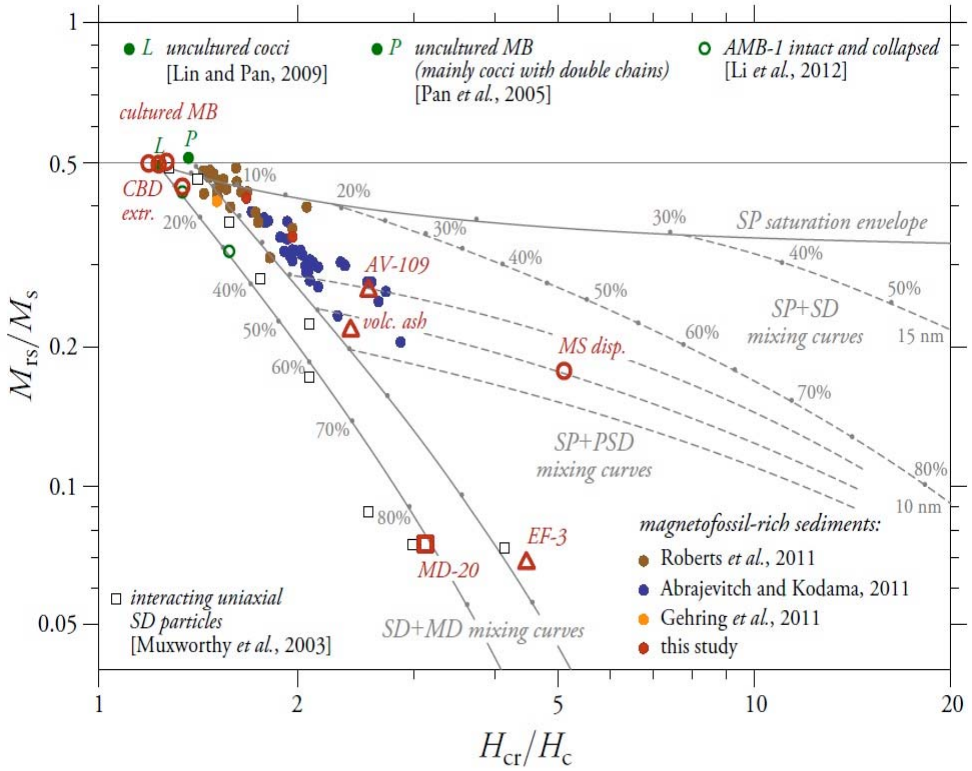

Fig. 8. Day diagram summarizing the hysteresis properties of samples discussed in this paper (red circles for SD samples, red triangles for PSD samples, red squares for MD samples), compared with properties of magnetofossil-bearing sediments (colored dots). The Day diagram with mixing curves between domain states (gray) is drawn from *Dunlop* [39]. Cultured magnetotactic bacteria (cultured MB) plot exactly on the expected spot for non-interacting uniaxial SD particles. The effect of magnetostatic interactions on such particles is shown with models from *Muxworthy et al.* [51] and with disrupted magnetosome chains (green circle, from [*52*]). In general, interacting SD particles follow the SD+MD mixing curve. Magnetofossil-bearing sediments follow a different trend with end-members defined by CBD-extractable magnetic minerals on the one hand (red circle labeled as "CBD extr.", from *Ludwig et al.* [30]) and the central region of the diagram on the other hand, possibly represented by a clay mineral dispersion of SDS-treated *Magnetospirillum* cells (red circle labeled as "MS disp."). Iron nanodots with single-vortex states (red triangle labeled as AV-109, from *Winklhofer et al.* [20]) do not plot on the expected trend line for PSD particles

along continuous segments of the magnetization curves. Each magnetization jump along the upper hysteresis branch is the starting point of a FORC that does not coincide with the previous one, while all FORCs starting from the same continuous hysteresis segment are identical.

Non-interacting, uniaxial SD particles have relatively simple FORC properties. First, no switching occurs when the field is reduced from positive saturation to zero. Therefore, all FORCs $M(H_r \geq 0, H)$ starting at positive reversal fields are identical to the upper branch M_+ of the major hysteresis loop and their shape is entirely determined by reversible magnetic moment rotation. Departure from M_+ of the FORC $M(0, H)$ originating at $H_r = 0$ (called saturation initial curve M_{si}), can be used as a measure of how much real hysteresis loops differ from the ideal non-interacting SD

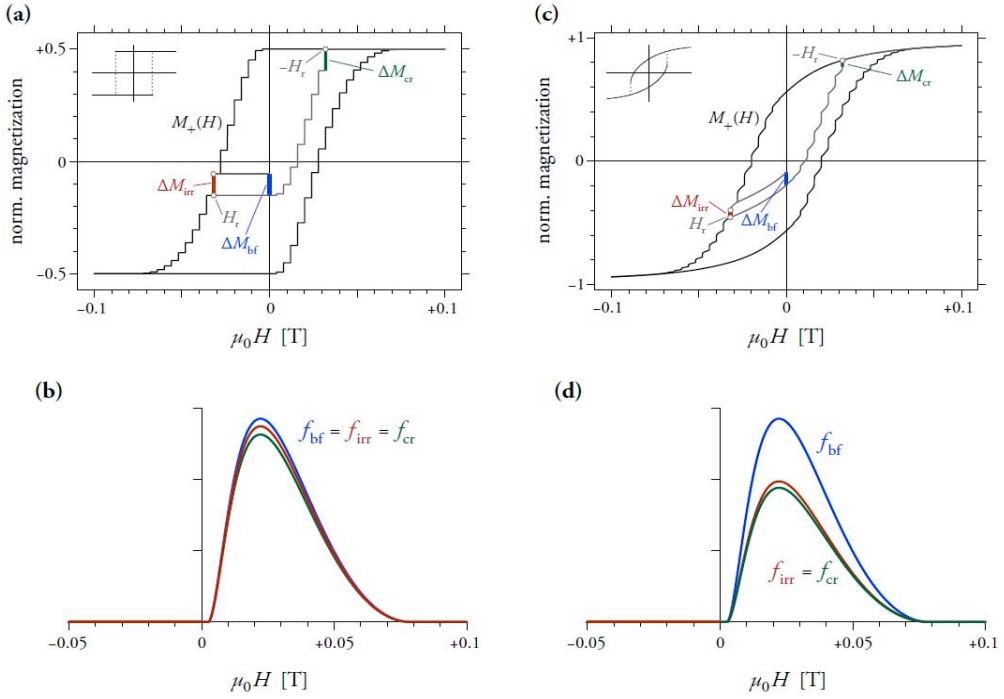

Fig. 9. Modeled FORC properties of few uniaxial, non-interacting SD particles. Switching of individual particles appears as magnetization jumps. (a) Preisach–Néel model with rectangular single particle hysteresis loops (inset). This case is characterized by $\Delta M_{irr} = \Delta M_{bf} = \Delta M_{cr}$, so that the coercivity distributions in (b) are identical. ΔM_{irr} and ΔM_{cr} are magnetization jumps produced by the same particle in H_r and $-H_r$, respectively. **(c)** Model with Stoner–Wohlfarth single particle hysteresis loops (inset). Magnetization jumps occur at the same fields as in (a), but their size is smaller, because magnetization changes are caused in part by magnetic moment rotations over the continuous segments. Because magnetization jump sizes of single particle hysteresis loops are smaller than saturation remanent magnetizations, $\Delta M_{irr} = \Delta M_{cr} < \Delta M_{bf}$, and the backfield coercivity distribution is larger than the other two coercivity distributions, as shown in (d)

case characterized by $M_{si} = M_+$ [49]. As soon as negative fields are reached along $M_+(H_r)$, all particles with $H_s > -H_r$ are switched: accordingly, FORCs starting at $H_r < 0$ are produced by a mixture of switched and unswitched particles. While the applied field is increased from $H_r < 0$ to $H = 0$, magnetic moments rotate reversibly without further switching. Moreover, the remanent magnetization $M_{bf} = M(H_r, 0)$ obtained at $H = 0$ reflects the same configuration of switched particles created at the beginning of the corresponding FORC.

In both examples of Fig. 9, the last magnetization jump of each FORC contributes to the central ridge and has the same amplitude as the magnetization jump on $M_+(H)$ from which the FORC is branching, because both jumps are produced by the two switching fields H_s of the same particle. Therefore, the coercivity distributions associated with $M_+(H_r)$ and with the central ridge are identical, i.e. $f_{cr}(x) = f_{irr}(x)$ over $x \geq 0$ and $f_{irr}(x < 0) = 0$ (Fig. 9b, d). The backfield coercivity distribution, on the other hand, is based on magnetization differences measured

in zero field instead of the switching fields, and is therefore distinct from the other two coercivity distributions in case of SD particles with curved elemental hysteresis loops, such as Stoner–Wohlfarth particles (Fig. 9c, d). In case of randomly oriented Stoner–Wohlfarth particles, the mean size of magnetization jumps in single-particle hysteresis is $\overline{S} = M_{\mathrm{irs}}/M_{\mathrm{rs}} = M_{\mathrm{cr}}/M_{\mathrm{rs}} = 0.5436$ [12], and $M_{\mathrm{rs}}/M_{\mathrm{s}} = 0.5$. Single-particle hysteresis loops become much closer to rectangular loops as soon as thermal activations are taken into consideration, because switching occurs in smaller fields where reversible magnetic moment rotation is less pronounced. FORC measurements yield $\overline{S} \approx 0.8$–0.9 for SD particles in a pelagic carbonate [30].

The FORC properties discussed above are important for the identification of SD particles in geologic samples, notably magnetofossils in freshwater and marine sediment, but also well-dispersed SD particles in rocks. In particular, the occurrence of sedimentary SD particles in isolated form or as linear chains produced by magnetotactic bacteria is the matter of an ongoing debate. For example, the unusually strong SD signature of sediments from the Paleocene–Eocene thermal maximum (PETM) has been attributed to magnetofossils produced by magnetotactic bacteria thriving in a particularly favorable environment [53, 54], as well as, at least in part, to isolated SD particles produced by a cometary impact [55]. In the following, some examples of FORC and coercivity distribution signatures of sedimentary SD particles are discussed.

The first example is based on high-resolution FORC measurements by *Wang et al.* [55] of a pure culture of the magnetotactic bacterium MV-1, which produces single chains of prismatic $\sim 35 \times 53$ nm magnetite crystals [56]. The original measurements have been reprocessed with VARIFORC and results are shown in Fig. 10. Isolated magnetosome chains behave as a whole like SD particles with uniaxial anisotropy, because the magnetic moments of individual crystal are switched in unison due to strong magnetostatic coupling [12, 57]. Magnetostatic interactions between chains, on the other hand, are minimized by the good separation naturally provided by the much larger cell volume.

Because of intrinsic magnetosome elongation and well-constrained dimensions, MV-1 cultures provide a close analogue to random dispersions of nearly identical, uniaxial SD particles. The resulting coercivity distributions are relatively narrow with virtually no contributions at $H_{\mathrm{c}} = 0$ (Fig. 10f), as expected for SD particles with minimum uniaxial anisotropy provided by crystal elongation and chain geometry. Hysteresis parameters ($M_{\mathrm{rs}}/M_{\mathrm{s}} = 0.496$, $H_{\mathrm{cr}}/H_{\mathrm{c}} = 1.19$, Fig. 8) practically coincide with those of randomly oriented Stoner–Wohlfarth particles. Lack of strong magnetostatic interactions is confirmed by the negligible intrinsic vertical extension, as predicted by theoretical calculations [11]. Ideally, the three types of coercivity distributions shown in Fig. 10f should be characterized by $f_{\mathrm{irr}} \equiv f_{\mathrm{cr}} \le f_{\mathrm{bk}}$ and $f_{\mathrm{irr}}(x) = 0$ for negative arguments, so that $M_{\mathrm{cr}}/M_{\mathrm{irs}} = 1$. The measured ratio $M_{\mathrm{cr}}/M_{\mathrm{irs}} = 0.64$ reflects residual FORC contributions of unspecified nature clearly visible over $H_{\mathrm{b}} > 0$, where $\rho = 0$ is expected from non-interacting SD particles [11]. These contributions are probably associated with a small fraction of collapsed magnetosome chains (Fig. 10d).

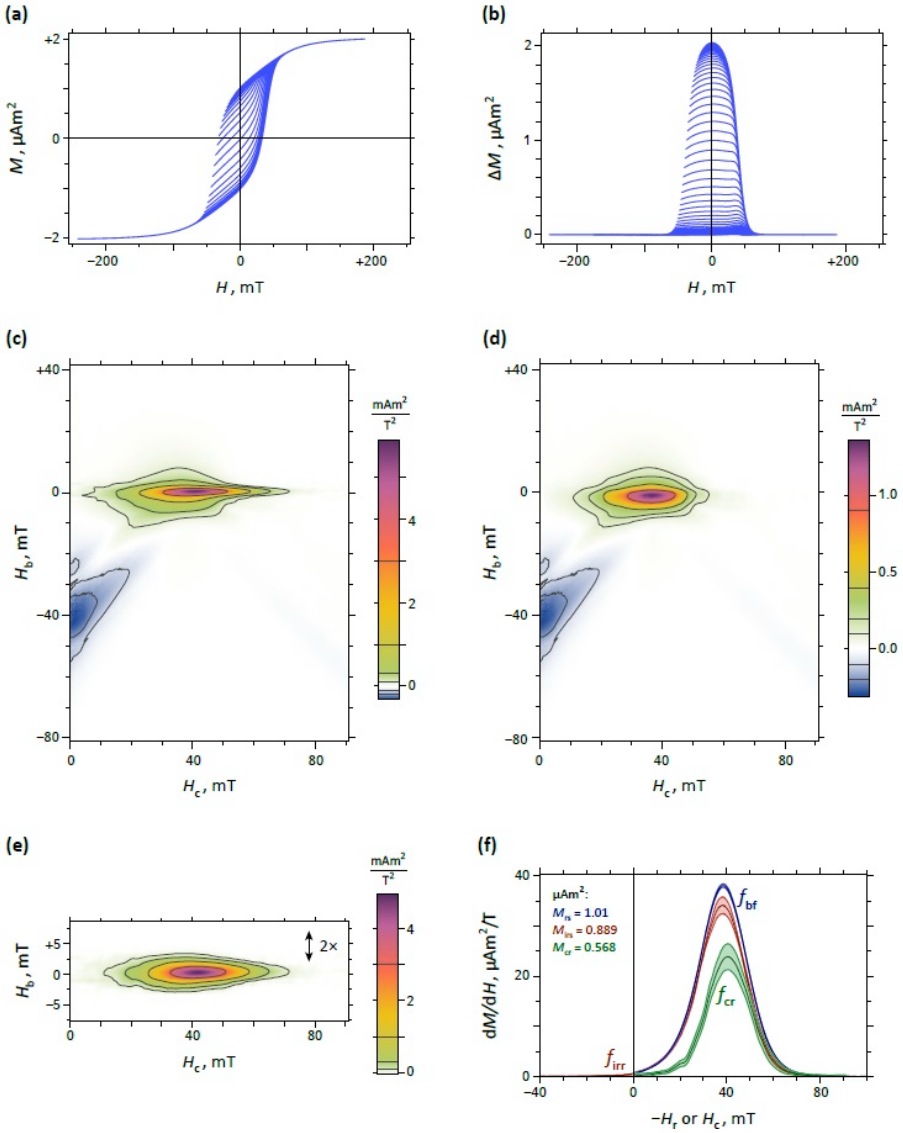

Fig. 10. Cultures of the magnetotactic bacterium MV-1 represent one of the best material realizations of non-interacting SD particle assemblages with minimum uniaxial magnetic anisotropy. These bacteria contain a single chain of SD magnetite crystals that switch in unison, behaving effectively as an equivalent SD particle with elongation along the chain axis. (a) Set of FORC measurements where every 4th curve is plotted for clarity. (b) Same as (a), after subtracting the lower hysteresis branch from each curve. Every 2nd curve is shown for clarity. The bell-shaped envelope of all curves is the difference between upper and lower hysteresis branches, i.e. the even component $M_{\rm rh} = (M_+ - M_-)/2$ of the hysteresis loop multiplied by a factor 2 [10]. (c) FORC diagram calculated with VARIFORC from the measurements shown in (a). (d) Same as (c), after subtraction of the central ridge. Most contributions in this diagram are due to reversible magnetization processes (i.e. in-field magnetic moment rotations). (e) Central ridge isolated from (c) and plotted with a 2× vertical exaggeration. Zero-coercivity contributions are completely absent, as expected for a system of particles with an intrinsic shape anisotropy along the chain axes. The central ridge's vertical extension slightly exceeds the minimum extension expected from data processing of an ideal ridge, revealing residual magnetostatic interactions between magnetosome chains. The associated interaction field amplitudes are <0.5 mT. (f) Coercivity distributions derived from FORC measurements and corresponding magnetizations calculated by integration of the distributions over all fields. The condition $M_{\rm irs} = M_{\rm cr}$ expected for these particles is not exactly met, because of residual FORC

contributions not corresponding to non-interacting, uniaxial SD particles. On the other hand, $f_{\mathrm{irr}}(x<0)=0$, as expected from positively saturated SD particles that cannot be switched in positive fields. High-resolution FORC measurements have been kindly provided by *Wang et al.* [55]

The second example is based again on a magnetotactic bacteria sample, but its magnetic properties are less straightforward. The sample is a synthetic sediment analogue obtained by dispersing cultured cells of the magnetotactic bacterium *Magnetospirillum magnetotacticum* MS-1 in a clay slurry (kaolinite) while dissolving the cell material with addition of 2% sodium dodecyl sulfate during continuous stirring. The purpose of this experiment was to check the stability of magnetosome chains in sediment once the cell material has been dissolved. Analogous experiments performed directly in aqueous solution yielded strongly interacting magnetosome clusters [58]. FORC analysis of this sample (Fig. 11) poses a formidable problem in terms of data processing, because of the simultaneous presence of (1) a sharp superparamagnetic (SP) overprint, and (2) a double discontinuity at $H_{\mathrm{r}}=H=0$, due to the simultaneous existence of a central ridge and a vertical ridge in the FORC diagram.

Because the sigmoidal SP overprint extends only over few measurement points, saturating in < 2 mT (Fig. 11a), it cannot be adequately fitted by polynomial regression with smoothing factors required for adequate measurement noise suppression [29]. The SP overprint is eliminated by subtracting the lower branch of the major hysteresis loop from all curves, in which case no particular features are seen at $H=0$ (Fig. 11b). This operation does not affect FORC calculations, because the H_{r}-derivative of any magnetization curve added or subtracted to all measurements is zero. For this reason, subtraction of the lower hysteresis branch is an option provided by VARIFORC for processing quasi-discontinuous measurements. Moreover, FORC measurement differences reveal details that are often completely hidden in hysteresis loops with $M_{\mathrm{rs}}/M_{\mathrm{s}}\to 0$ and/or large paramagnetic contributions.

The hysteresis loop of this sample is clearly constricted at $H=0$, in what is often called a 'wasp-waisted' shape [59]. The interpretation of corresponding Day diagram parameters ($M_{\mathrm{rs}}/M_{\mathrm{s}}=0.177$, $H_{\mathrm{cr}}/H_{\mathrm{c}}=5.12$, Fig. 8) is ambiguous, involving mixtures of SD, PSD, and SP particles. On the other hand, the FORC diagram (Fig. 11c), contains two precisely interpretable signatures, namely a central ridge, as expected for non-interacting SD particles, and a vertical ridge due to magnetic viscosity. Additional FORC contributions outside of the two ridges are very weak (Fig. 11d). Coercivity distributions (Fig. 11f) are characterized by an exponential-like functions peaking at $H_{\mathrm{c}}=0$. Because this is also true for f_{cr}, many particles must have vanishingly small switching fields. Such features can be explained by a combination of thermal activation effects and the absence of chain-derived uniaxial anisotropy, as expected for equidimensional MS-1 magnetosomes if their original arrangement is destroyed. On the other hand, the presence of magnetosome clusters similar to those obtained from cell disruption in aqueous solutions [58] can be excluded, because of the absence of magnetostatic interaction signatures otherwise reported with FORC diagrams of extracted magnetosomes [e.g. 55, 60]. The apparent contradiction between lack of uniaxial chain anisotropy and magnetostatic interaction signatures can be reconciled by assuming that magnetosomes have been individually dispersed in the clay matrix.

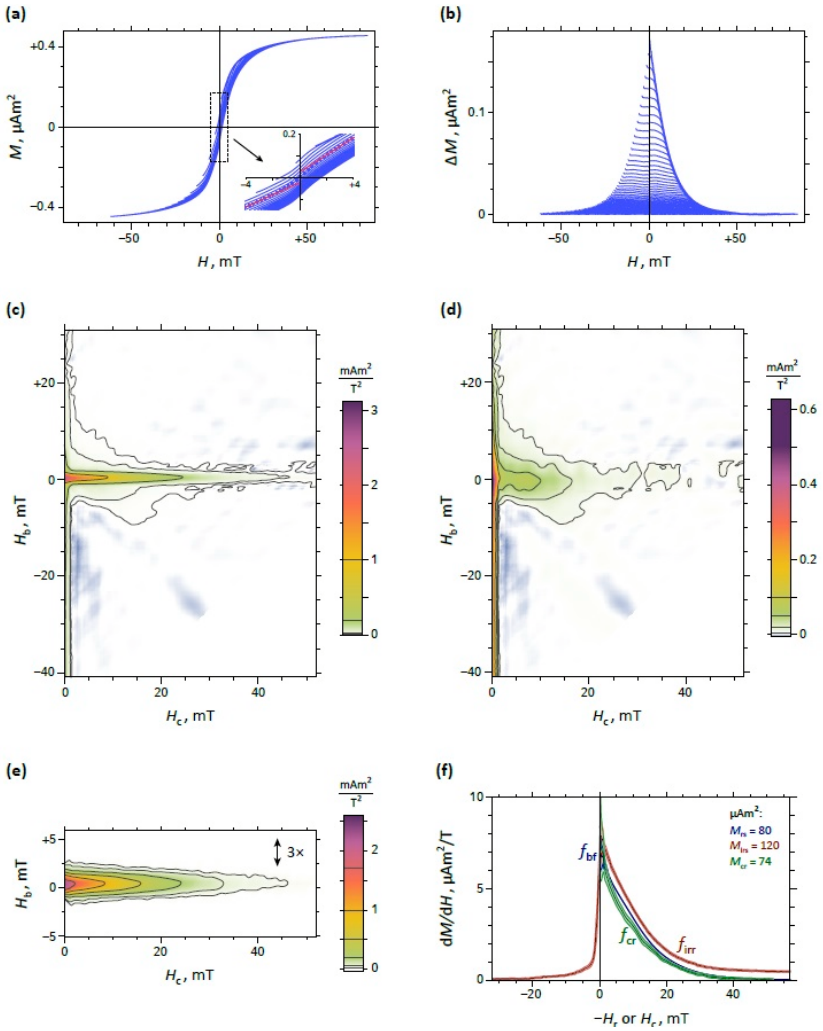

Fig. 11. FORC measurements of a specially prepared sample containing equidimensional magnetite magnetosomes. The sample was obtained by dispersing a *Magnetospirillum* culture in clay (kaolinite) with subsequent 2% SDS addition under continuous stirring. Dissolution of cell material by SDS is expected to produce clay-magnetosomes aggregates of some form. (a) Set of FORC measurements where every 12th curve is plotted for clarity. The insert shows a zoom around the origin, where a sigmoidal SP contribution is recognizable. The SP signature saturates in <2 mT, and, although not contributing to the FORC diagram, it poses a processing problem, because polynomial regression provides a correct fit only if unsuitably small smoothing factors are chosen (SF = 2 in this case). (b) Same as (a), after subtracting the lower hysteresis branch from each curve. Every 3rd curve is shown for clarity. The exponential-like envelope of all curves is the difference between the upper and lower hysteresis branches, and the cusp at $H = 0$ denotes a system with zero-coercivity contributions. The SP contribution shown in the inset of (a) is naturally eliminated from measurement differences, which therefore no longer pose FORC processing problems. (c) FORC diagram calculated with VARIFORC from the measurement differences shown in (b). The only significant contributions are the central ridge, indicative of non-interacting SD particles, and a vertical ridge at $H_c = 0$, which is produced by magnetic viscosity. The absence of other significant FORC contributions, and in particular the typical signature for reversible magnetic moment rotation, indicate that single-particle hysteresis loops are practically rectangular. (d) Same as (c), after subtraction of the central ridge. Residual contributions around the former central ridge location reveal additional magnetization processes, which, given the SD nature of the sample, must arise from magnetostatic interactions. (e) Central ridge isolated from (c) and plotted with a 3× vertical exaggeration. The central ridge peak at $H_c = 0$ denotes a system containing SD particles with vanishing coercivity. (f)

Coercivity distributions derived from FORC measurements and corresponding magnetizations calculated by integration of the distributions over all fields. The condition $M_{irs} \approx M_{rs} \approx M_{cr}$ met by this sample is typical for non-interacting SD particles with squared hysteresis loops and represents a physical realization of a Preisach–Néel system. Residual f_{irr} contributions over negative arguments are caused by non-zero FORC amplitudes over $H_b > 0$ in (d)

The three coercivity distributions derived from FORC measurements are almost identical; approaching the limit case $f_{bk} \equiv f_{cr} \equiv f_{irr}$ predicted for non-interacting SD particles with rectangular single-particle hysteresis loops. Rectangular loops can be explained by the strong switching field reduction in thermally activated SD particles close to the SD/SP threshold. This example demonstrates the level of detailed information that is provided by high-resolution FORC measurements. Results shown in Fig. 10 and Fig. 11 can be considered representative for well dispersed SD particles with and without minimum uniaxial shape anisotropies. The effect of shape anisotropy is much less evident with samples of interacting SD particles, because local interaction fields act as an additional magnetic anisotropy source.

The third SD example is based on high-resolution FORC measurements of a magnetofossil-bearing pelagic carbonate from the Equatorial Pacific [30]. Typical sediment magnetizations of the order of few mAm^2/kg, as for this sample, yield FORC measurements with important noise contributions that need to be adequately suppressed in order to obtain useful FORC diagrams. FORC processing becomes critical in such cases, as shown in Fig. 12. Conventional data processing based on constant smoothing factors yields significant values of the FORC distribution only over a limited region around the central ridge (Fig. 12a), unless the high resolution required in proximity of $H_b = 0$ and $H_c = 0$ is sacrificed. The VARIFORC variable smoothing algorithm, on the other hand, finds a locally optimized compromise between resolution preservation and noise suppression. With this approach, significant domains of the FORC distribution are dramatically expanded (Fig. 12b), revealing a broad, continuous background around the central ridge, as well as negative FORC amplitudes characteristic for SD particles.

The last example of this section (Fig. 13) is based on a special technique used to isolate the contribution of secondary SD magnetite particles from the same pelagic carbonate sample of Fig. 12. For this purpose, identical FORC measurements has been performed before and after treating homogenized sediment material with a citrate-bicarbonate-dithionite (CBD) solution for selective magnetofossil dissolution [30]. Large magnetite crystals, as well as SD particles embedded in a silicate matrix, are not affected by this treatment. Therefore, differences shown in Fig. 13 between the two sets of measurements represent the intrinsic magnetic signature of CBD-extractable particles. Hysteresis properties ($M_{rs}/M_s = 0.44$, $H_{cr}/H_c = 1.34$, Fig. 8) are close to the limit case of randomly oriented, non-interacting SD particles with uniaxial anisotropy, despite evident magnetostatic interaction signatures deducible from positive FORC contributions over the upper quadrant (Fig. 13d). Interpretation of interaction signatures in terms of collapsed magnetosome chains or authigenic SD magnetite clusters requires further investigation [30]. Coercivity distributions (Fig. 13f) display minor contributions near $H_c = 0$, and their overall shape is better associable with intact

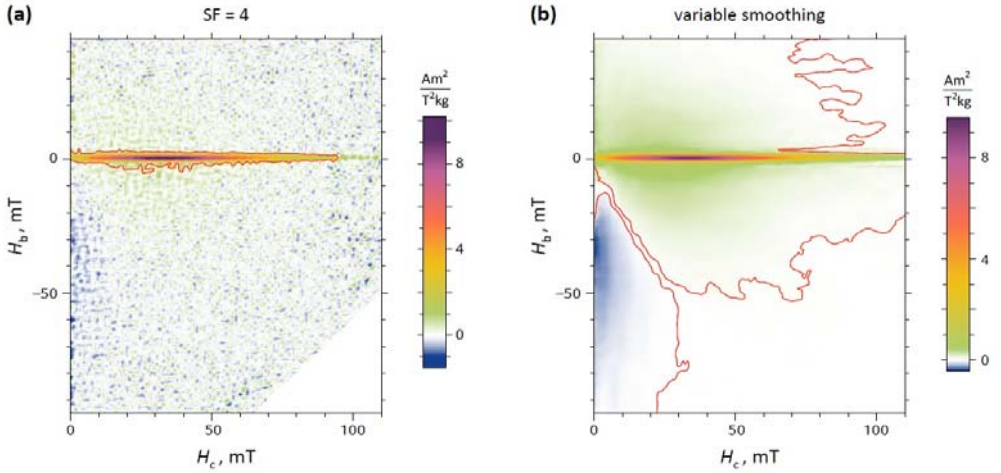

Fig. 12. Example showing the importance of proper FORC processing for extracting detailed information from weak natural samples. The two FORC diagrams have been obtained from the same set of high-resolution measurements (field step size: 0.5 mT) of a pelagic carbonate from the Equatorial Pacific [30]. The red contour(s) enclose significant regions of the FORC diagram, i.e. regions where the FORC function is not zero at a 95% confidence level according to the error calculation method implemented by *Heslop and Roberts* [35]. (a) Conventional FORC processing with a constant smoothing factor SF = 4. The central ridge is the only significant FORC feature that can be resolved. Larger smoothing factors would extend the significant region at the cost of blurring the central ridge to the point where it can no longer be identified as such (see Fig. 1 in *Egli* [29]). (b) VARIFORC processing obtained with a variable smoothing factor optimized for the best compromise between noise suppression and detail preservation. Low-amplitude features, such as negative contributions, are now significant over large portions of the whole FORC space

magnetotactic bacteria cultures (Fig. 10) than dispersed magnetosomes in clay (Fig. 11). Coercivity distributions of magnetofossil-bearing sediment are wider than those of individual bacterial strains, because of the natural diversity of magnetosome and chain morphologies. On the other hand, no systematic differences are observed between FORC-related magnetization ratios (Table 1), as long as chain integrity is not evidently compromised. In particular, FORC properties of PETM sediment appear to be compatible with those of similar magnetofossil-bearing samples, rather than dispersions of equidimensional SD particles.

3.2. PSD magnetic assemblages. The next two FORC examples are based on PSD particle assemblages, starting with the simplest case of an array of identical, weakly interacting Fe nanoparticles with grain sizes slightly larger than the upper SD limit [20]. These particles can have two pairs of antiparallel magnetic states: so-called 'flower' states with nearly homogenous magnetization and SD-like magnetic moments (SD_+ and SD_-), and single vortex states with nearly zero magnetic moments (SV_+ and SV_-). Hysteresis properties are shaped by the transition sequences $SD_+ \rightarrow SV_+ \rightarrow SD_-$ and $SD_- \rightarrow SV_- \rightarrow SD_+$ between positive and negative saturation. Similar transitions in magnetite cubes have been modeled micromagnetically [61], yielding the single-particle hysteresis loops shown in Fig. 14.

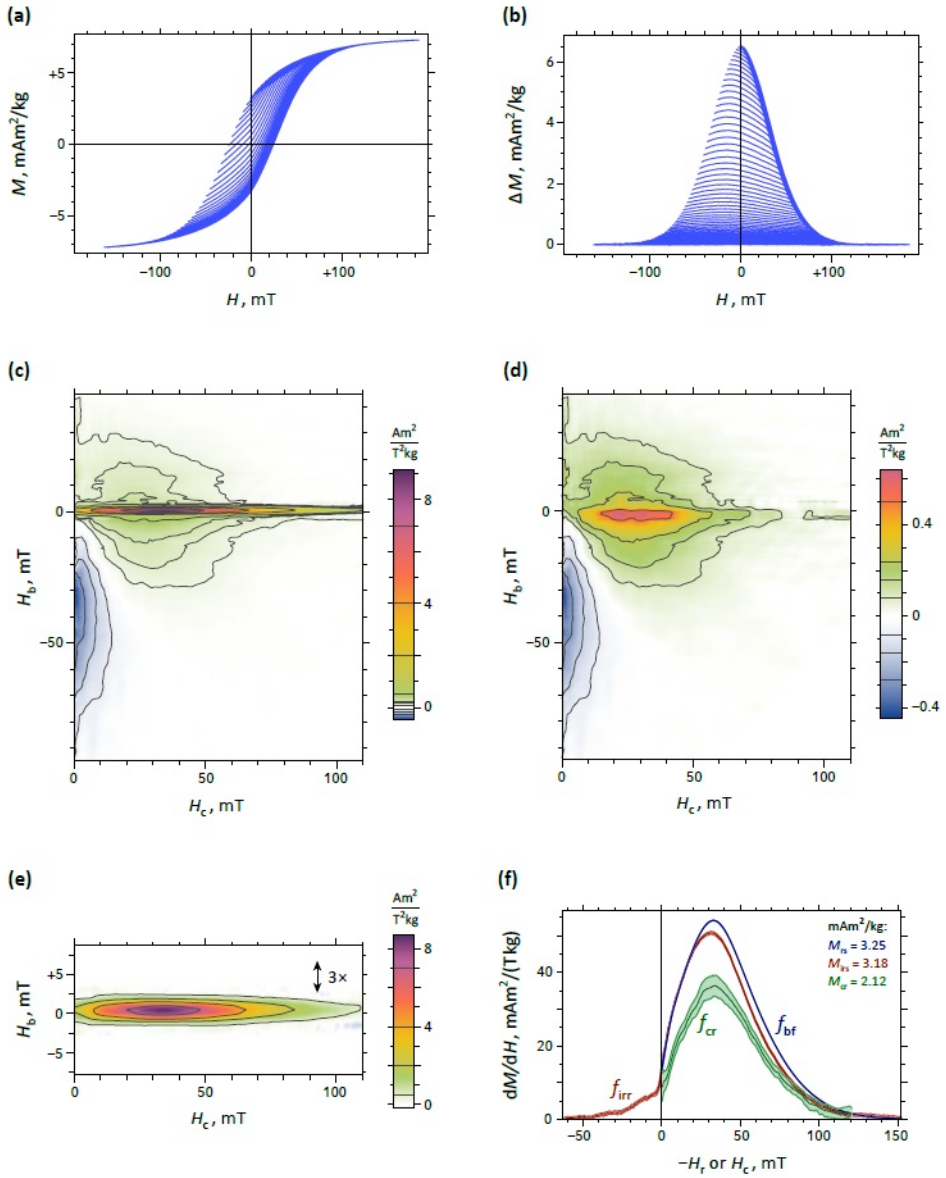

Fig. 13. FORC analysis of a pelagic carbonate sample from the Equatorial Pacific, obtained from differences between identical measurements of the same material before and after selective SD magnetite dissolution of [30]. This approach, combined with the fact that the main magnetization carriers are magnetofossils, ensures that the results shown here represent the uncontaminated signature of secondary SD minerals. (a) Set of FORC measurements where every 8th curve is plotted for clarity. (b) Same as (a), after subtracting the lower hysteresis branch from each curve. Every 4th curve is shown for clarity. The bell-shaped envelope of all curves is the difference between the upper and lower hysteresis branches. Its shape is intermediate between the examples shown in Figs. 10–11, but closer to Fig. 10. (c) FORC diagram calculated with VARIFORC from the measurements shown in (a). The central ridge is overlaid to additional low-amplitude contributions (<10% of the central ridge peak), which, because of their extension over the FORC space, represent as much as ~50% of the total magnetization M_{irs} 'seen' by the measurements. (d) Same as (c), after subtraction of the central ridge. The lower quadrant partly coincides with the signature of reversible magnetic moment rotations as predicted by *Newell* [11]. Because non-SD contributions are excluded by the special preparation procedure, positive FORC amplitudes over $H_{\mathrm{b}} > 0$ must represent the signature of magnetostatic interactions between SD particles. (e) Central ridge

isolated from (c) and plotted with a 3× vertical exaggeration. (f) Coercivity distributions derived from FORC measurements and corresponding magnetizations calculated by integration of the distributions over all fields. Relative contributions of the three types of magnetizations are similar to those of the MV-1 example in Fig. 10

Tab. 1

Hysteresis parameters H_{cr}/H_c and M_{rs}/M_s, ratios between FORC-derived magnetizations M_{rs}, M_{irs}, and M_{cr}, for samples described in this paper

Material	H_{cr}/H_c	M_{rs}/M_s	M_{irs}/M_{rs}	M_{cr}/M_{rs}	M_{cr}/M_{irs}
Strictly SD examples					
MS-dispersion	5.12	0.177	1.397	0.885	0.633
MS-1	1.233	0.494	0.928	0.510	0.550
AMB-1 [a]	1.267	0.500	0.893	0.698	0.782
MV-1 [b]	1.190	0.496	0.879	0.561	0.638
SD in pelagic carbonate [c]	1.340	0.442	0.815	0.651	0.667
Magnetofossil-rich sediment					
Pelagic carbonate [c]	1.690	0.399	1.011	0.569	0.563
PETM [b]	1.677	0.418	0.953	0.550	0.576
Soppensee [d]	1.503	0.411	1.066	0.387	0.364
PSD particles					
AV-109 [e]	2.578	0.267	1.856	0.598	0.322
EF-3	4.489	0.069	2.500	0.097	0.039
Volcanic ash [b]	2.421	0.219	1.976	0.024	0.012
MD particles					
MD20	3.147	0.075	2.873	~0	~0

[a] FORC data kindly provided by *Li et al.* [52].
[b] FORC data kindly provided by *Wang et al.* [55].
[c] FORC data from *Ludwig et al.* [30].
[d] FORC data from *Kind et al.* [70].
[e] FORC data from *Winklhofer et al.* [20].

The complex FORC signature of Fe nanoparticles (Fig. 15) can be explained by a combination of the two micromagnetic models in Fig. 14, with individual peaks corresponding to magnetic transitions between SD and SV states. The $SV_- \rightarrow SD_+$ transition along the lower hysteresis branch produces a central ridge peaking at $H_c \approx 0.15$ T. Additional pairs of positive FORC peaks at $H_c \approx 0.06$ T and negative peaks just above and below the central ridge are produced by the remaining transitions, while negative FORC amplitudes peaking at $H_b \approx -0.15$ T can be explained by reversible magnetization changes of the SV_+-state in proximity of its denucleation field. All relevant FORC contributions occur at or in proximity of SV nucleation in ±0.01 T and SV denucleation in ±0.15 T (Fig. 15c), producing a constricted hysteresis loop (Fig. 15a) and bimodal coercivity distributions (Fig. 15f).

Unlike the case of isolated SD particles, magnetic state transitions from positive saturation (i.e. SD_+) occur already in positive fields. These transitions (e.g. SV nucleation) are not captured by remanent demagnetization measurements, therefore contributing to $f_{irr}(x<0)$, but not to f_{bk}. In the example of Fig. 15, SV denucleation is the only process captured by the central ridge, so that f_{cr} is characterized by a single peak at $H_c \approx 0.15$ T, instead of two peaks as for the other two coercivity distributions.

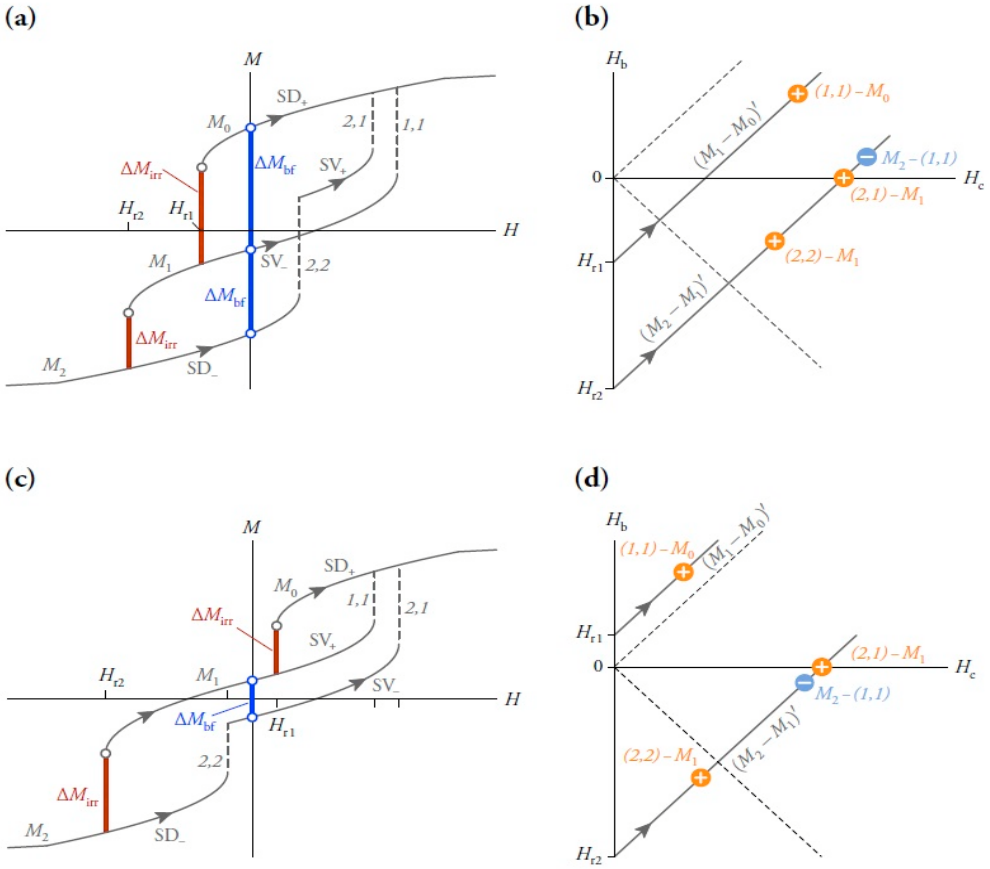

Fig. 14. Two examples of single particle hysteresis loops (left plots) and corresponding FORC diagrams (right plots), generated by micromagnetic simulations of 0.1 μm (a) and 0.11 μm (c) magnetite cubes by *Newell and Merrill* [61]. In both cases, the particles have two SD-like ($SD_{\pm}$) and two vortex-like ($SV_{\pm}$) magnetization states. SD-like states in (c) exist only in sufficiently large applied fields and cannot contribute to remanent magnetizations. Transitions between magnetic states occur at magnetization jumps (dashed lines and red lines), defining three groups of identical FORCs M_0, M_1 and M_2. Magnetization jumps relevant for FORC calculations are labeled by number pairs like in Fig. 3. Corresponding positive and negative peaks of the FORC function (b, d) are shown with '+' and '–' symbols, respectively. Gray diagonal lines with arrows are the only FORC trajectories producing non-zero contributions. Only peaks located to the right of the dashed lines contribute to the backfield demagnetization curve and thus to M_{rs}, determining large differences in magnetic remanence properties of otherwise similar FORC diagrams.

Hysteresis parameters of small PSD crystals are very sensitive to vortex nucleation fields: if nucleation from positive saturation occurs in negative fields, SD-like values of M_{rs}/M_s are obtained from SD states that are stable in zero fields. If, on the contrary, vortex states can nucleate from SD_+ in positive fields, M_{rs}/M_s drops well below 0.5, because of their small net magnetic moment. On the other hand, PSD particles are always characterized by $M_{cr} < M_{bk} < M_{irs}$, unlike the case of non-interacting SD particles, where $M_{bk} \geq M_{irs}$.

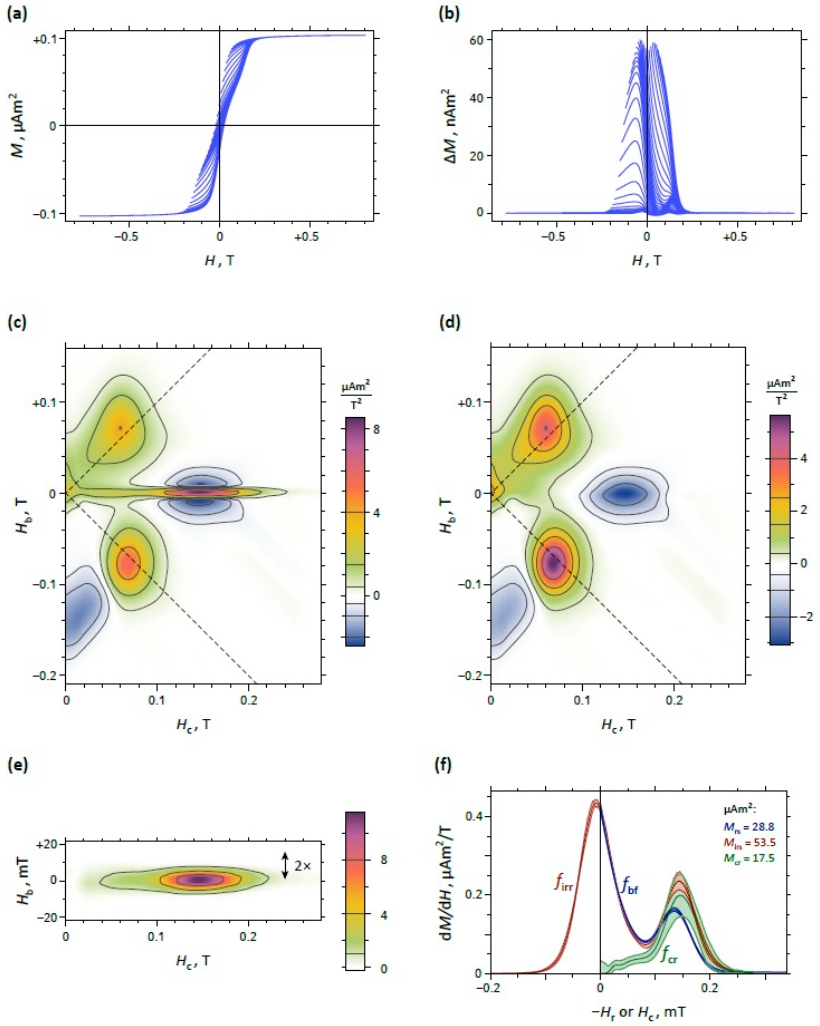

Fig. 15. FORC analysis of Fe nanodots [20]. The artificial sample (AV-109) is a two-dimensional, quasi-hexagonal array of polycrystalline Fe nanodots with a diameter of 67 ± 13 nm and 20 nm thickness. The nanodots center-to-center spacing is ~2 dot diameters [62]. FORC measurements have been performed in the array plane. (a) Set of FORC measurements where every 2nd curve is plotted for clarity. (b) Same as (a), after subtracting the lower hysteresis branch from each curve. Every 2nd curve is shown for clarity. Hysteresis loop constriction at $H = 0$ and the double peak of the curve envelope in (b) are produced by a bimodal distribution of nucleation fields. As evident in (b), some FORCs cross each other, as well as the lower hysteresis branch. This means that regions outside the major hysteresis loop can in principle be accessed by FORC measurements (e.g. Fig. 14a), albeit rarely seen with natural samples and impossible with non-interacting SD particles. (c) FORC diagram calculated with VARIFORC from the measurements shown in (a), featuring localized peaks typical for magnetic transitions between four magnetic states: two SD-like states with large magnetic moments, and two states corresponding to a single magnetic vortex with small net magnetic moment. Because magnetic particles in this sample are practically identical, magnetic transitions occur collectively, appearing as distinct FORC function peaks. In case of less homogenous samples, FORC peaks would merge into a continuous background with triangular contour lines, as commonly seen with natural PSD assemblages. The dashed lines mark the rectangular domain of FORC amplitudes associated with remanent magnetizations. Accordingly, only about half of the two peaks at $H_c \approx 0.06$ T contribute to M_{rs}. (d) Same as (c), after subtraction of the central ridge. The two negative peaks around the central ridge in (c) now appear as a single contribution produced by vortex denucleation. (e) Central ridge isolated from (c) and plotted with a 2× vertical exaggeration, featuring a single peak at ~0.15 T. (f) Coercivity distributions derived

from FORC measurements and corresponding magnetizations calculated by integration of the distributions over all fields. The bimodal character of f_{irr} and f_{bf} arises from the existence of two different fields for nucleation (±0.01 T) and denucleation (±0.15 T) of vortex states, producing the constricted hysteresis loop seen in (a). Only vortex denucleation is captured by the central ridge, so that f_{cr} consists of a single peak

The FORC diagram in Fig. 15c does not resemble the typical signature of PSD magnetite in synthetic and geologic samples, which consists of a unimodal distribution peaking near $H_c = H_b = 0$, with triangular contour lines having their maximum vertical extension at $H_c = 0$ [24, 18]. This signature is explainable on the basis of the abovementioned PSD processes by taking the following factors into consideration: first, magnetic states of small PSD particles are very sensitive to grain sizes and shapes, so that magnetization jumps of single-particle hysteresis generate distinct FORC peaks only in case of exceptionally homogeneous samples, such as the Fe nanoparticles discussed above. Second, the number of possible magnetic states grows rapidly with increasing grain size, along with the number of FORC peaks, which eventually merge into a unimodal function. As discussed in Section 2, the FORC function occupies a triangular area of the FORC space limited by vertices with coordinates $(0,\pm H_{sat})$ and $(H_{sat},0)$, where H_{sat} is the field in which the two branches of the hysteresis loop merge. This limit is consequently imposed to the shape of contour lines. Finally, the central ridge is broadened by magnetostatic interactions, which are probably not negligible in most synthetic magnetite powders.

Some natural materials, such as olivine-hosted Fe–Ni particles in chondritic meteorites [63], contain weakly interacting PSD particles with sufficiently homogeneous properties for producing FORC diagrams with distinguishable contributions from vortex nucleation and denucleation. In such cases, high-resolution measurements are essential for capturing details of PSD magnetization processes. Faint evidence of such processes persists in FORC diagrams of many natural rocks (Fig. 16). Because of its sharpness, the central ridge remains distinguishable even when contributing to as low as few % of M_{irs}. Localized negative amplitudes over the lower quadrant, on the other hand, produce characteristic contour line indentations when overlaid to a positive background. Resolution of such signatures in PSD samples can benefit paleomagnetic applications, where FORC analysis has been proposed as a selection [64–66] and modeling [67, 68] tool for paleointensity determinations. For example, M_{cr}/M_{irs} is a measure for the relative magnetization of vortex states, which probably represent the preferential PSD contribution to natural remanent magnetizations.

3.3. MD particles. Domain wall displacement models [21, 22] explain the ideal hysteresis properties and FORC signature of MD particles (Fig. 4). These properties are met by annealed magnetite crystals [21], while FORC diagrams of unannealed particles (Fig. 17) can be explained by the superposition of MD and PSD signatures. As far as coercivity distributions are concerned, ideal MD properties are characterized by hysteresis branches and corresponding irreversible contributions being quasi-symmetric about $H = 0$, which means that $f_{irr}(x) \approx f_{irr}(-x)$. The typical f_{irr}-shape of MD particles resembles a Laplace (double exponential) distribution (Fig. 17c).

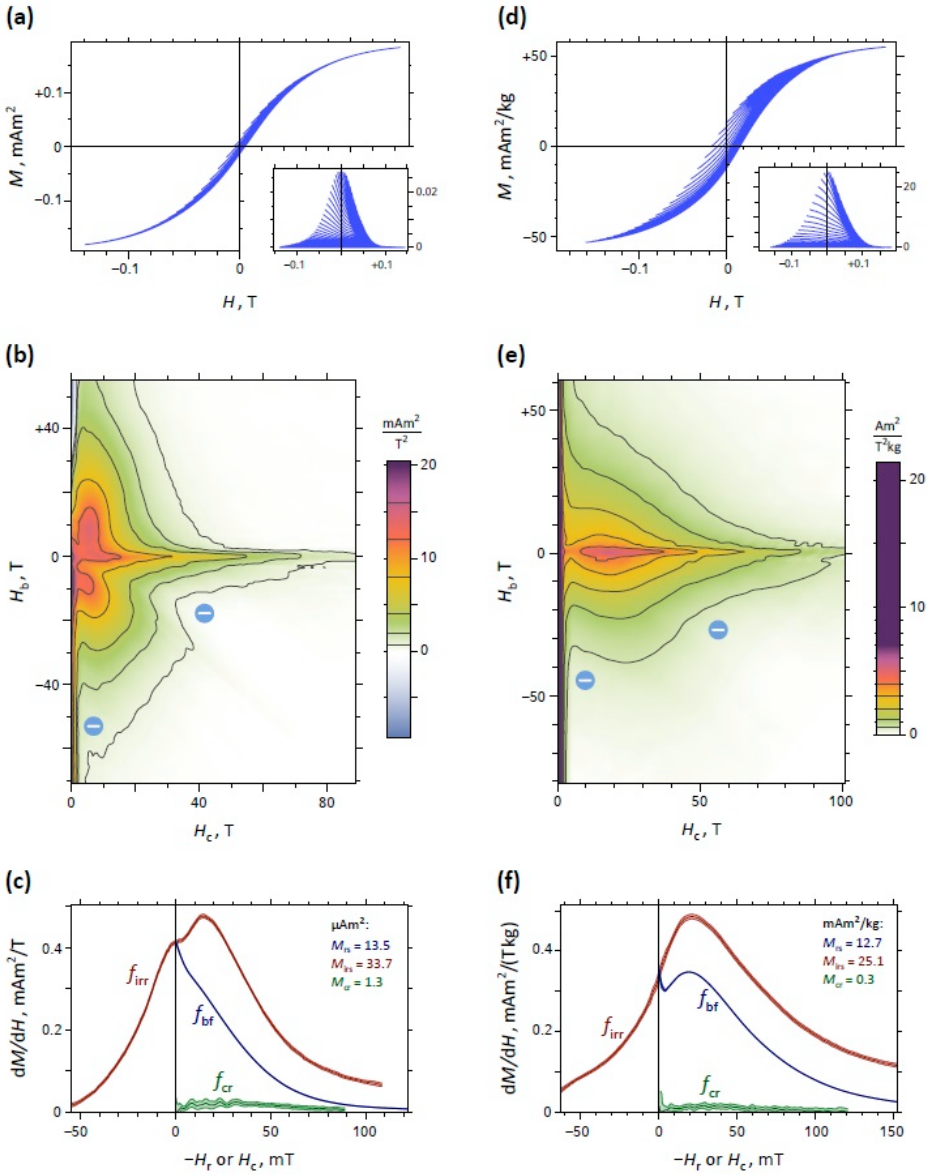

Fig. 16. Two FORC examples based on natural samples containing PSD particle assemblages, i.e. (a–c) basalt (sample EF-3), and (d–f) volcanic ash [30]. (a, d) FORC measurements, with results after lower hysteresis branch subtraction shown in the insets. (b, e) FORC diagrams calculated with VARIFORC from the measurements shown in (a, d). Some features typical of single-vortex PSD particles (Fig. 15) can be recognized, namely the existence of a central ridge, albeit much weaker, and the influence of localized negative FORC amplitudes (labeled with a minus sign) on the overall shape of contour lines. Furthermore, two nearly symmetric positive peaks above and below the central ridge are distinguishable in (b). Unlike in the example of Fig. 15, the existence of such contributions cannot be directly inferred from the hysteresis loop. The vertical ridge along $H_c = 0$ in (e) is a signature of magnetic viscosity. (c, f) Coercivity distributions derived from the FORC measurements shown in (b, e). Residual bimodality is still recognizable for f_{irr} and f_{bf} in (c). The central ridge distribution f_{cr} is much smaller than the other two, but significantly >0. Unlike the case of SD particles, the contribution of f_{irr} over negative arguments is not negligible, as expected from large positive FORC amplitudes over the upper quadrant

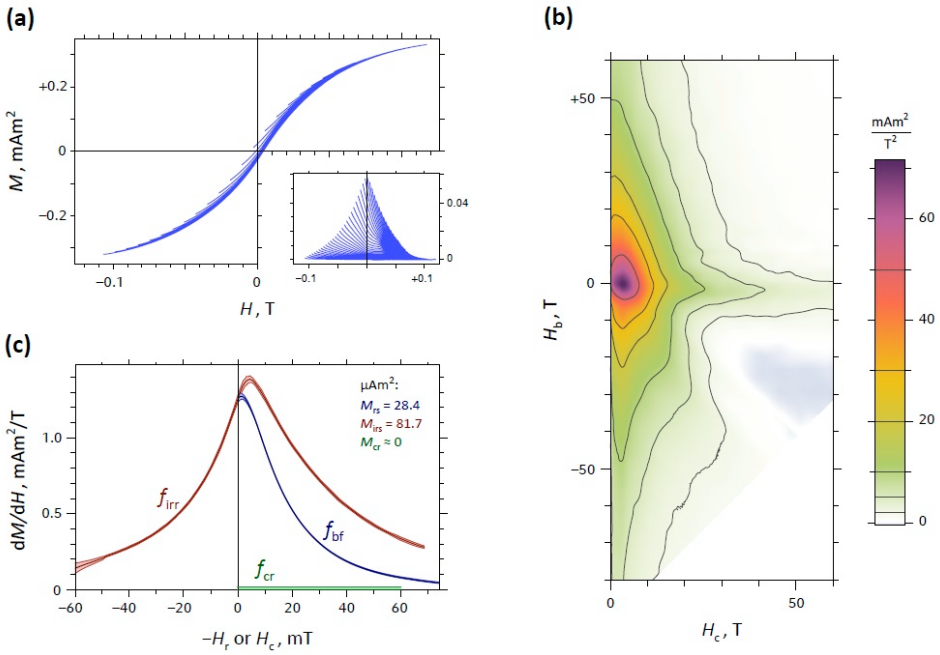

Fig. 17. FORC analysis of synthetic MD magnetite particles with 20–25 μm mean grain size. (a) Set of FORC measurements where every 8th curve is plotted for clarity. The inset shows the same set of curves (every 4th is plotted) after subtraction of the lower hysteresis branch. Measurement details are recognizable only in this plot, because of the very small hysteresis loop opening. (b) FORC diagram obtained with VARIFORC from the FORC measurements shown in (a). The MD nature of this sample is determined by the large vertical spread of the FORC function in proximity of $H_c = 0$. Additional PSD signatures are recognizable over $H_b < 0$ and along a sort of blurred central ridge. These features are typical of unannealed MD crystals. (c) Coercivity distributions derived from the FORC measurements shown in (c). f_{irr} is a quasi-even function with similar contributions over negative and positive field, as expected for MD particles. The central ridge does not exist, so that $f_{cr} = 0$

Because the magnetization of ideal crystals with weak domain wall pinning is almost completely reversible, irreversible processes, which occur in the form of so-called *Barkhausen magnetization jumps*, represent only a small fraction of the saturation magnetization, i.e. $M_{irs}/M_s \ll 1$. For example, $M_{irs}/M_s = 0.22$ for the 20–25 μm magnetite crystals of Fig. 17. Only a small fraction of all Barkhausen jumps yield a remanent magnetization, so that $M_{rs}/M_{irs} \ll 1$ ($M_{rs}/M_{irs} = 0.35$ for the example of Fig. 17). Since $f_{bk}(0) = f_{irr}(0)$, the backfield coercivity distribution is a function that decays much more rapidly than f_{irr} to zero for positive arguments. Finally, $f_{cr} = 0$ because of the absence of a central ridge.

In summary, ideal MD crystals without strong domain wall pinning are characterized by $M_{cr} = 0$ and $M_{rs} \ll M_{irs} \ll M_s$. For comparison, PSD and SD particles yield $M_{rs} < M_{irs}$ and $M_{rs} \geq M_{irs}$, respectively. Therefore, the ratio M_{rs}/M_{irs} can be considered as a sort of domain state indicator analogous to M_{rs}/M_s, with the important advantage that M_{rs}/M_{irs} is insensitive to reversible magnetization processes (e.g. SP contributions).

Conclusions

FORC diagrams are two-dimensional parameter representations of hysteresis processes providing a lot more details than the conventional bulk hysteresis parameters M_{rs}/M_s and H_{cr}/H_c. The simplest interpretation of FORC diagrams is based on Preisach theories, which, however, rarely describes real magnetization processes. Dedicated models have been developed for explaining the FORC properties of ideal SD, PSD, and MD particle assemblages. Such models describe 'end-member' FORC signatures that can be used for qualitative interpretation of FORC diagrams in terms of domain states. This has been the first rock magnetic application of FORC measurements. Meanwhile, continuous modeling improvements and the use of high-resolution measurements resulted in first quantitative FORC analyses of samples containing non-interacting SD particles.

An important forward step in FORC analysis consists in overcoming the quantitative gap with conventional magnetic parameters. As shown in this article, FORC measurements define three different types of irreversible magnetizations and corresponding coercivity distributions: the first type is represented by the well-known saturation remanence M_{rs} and associated coercivity distribution derived from backfield demagnetization. The second magnetization type defined by FORC measurements is the irreversible saturation magnetization M_{irs}, which is the sum of all irreversible magnetization changes occurring along the upper or lower branch of the hysteresis loop. M_{irs} is also the total integral of the FORC function. The coercivity distribution associated with M_{irs} represents irreversible processes occurring on the upper hysteresis branch at a given field. The third, so-called central ridge magnetization M_{cr} is generated by the last magnetization jump occurring in single particle hysteresis loops of isolated SD and small PSD magnetic particles. The central ridge coercivity distribution is derived from the corresponding signature of the FORC function along $H_b = 0$.

Unlike M_{rs}/M_s and H_{cr}/H_c, these magnetizations are unaffected by reversible magnetizations and provide more robust domain state information than the Day diagram. For example, the Day diagram characteristics of clay-dispersed, SDS-treated magnetosome chains (Fig. 8) suggest a mixture of SD, SP, and PSD particles. In reality, as seen with FORC diagram measurements, the whole remanent magnetization of this sample is produced by non-interacting SD particles. This sample represents a possible end-member of a trend defined by magnetofossil-bearing sediments on the Day diagram. The magnetic properties of these sediments are therefore not necessarily interpretable as mixtures of magnetofossils on the one hand, and SP and PSD particles on the other. Another example is represented by the Day diagram properties of small PSD particles (Fig. 15), which plots on the same trend defined by sediments, while its purely PSD nature is clearly recognizable on the basis of M_{irs}/M_{rs} and M_{cr}/M_{irs}.

All FORC processing aspects described in this paper, including the calculation of FORC-related magnetizations and coercivity distributions, have been implemented in the VARIFORC software package, so that they can become a routine magnetic analysis tool.

References

1. Chikazumi S. Physics of Ferromagnetism. N. Y., Oxford Univ. Press, 1997. 682 p.
2. Coey J.M.D. Magnetism and Magnetic Materials. Cambridge, Cambridge Univ. Press, 2010. – 625 p.
3. Dunlop D.J., Özdemir Ö. Rock Magnetism: Fundamentals and Frontiers. Cambridge, Cambridge Univ. Press, 1997. 594 p.
4. Tauxe L. Essentials of Paleomagnetism. Berkeley, University of California Press, 2010. 505 p.
5. Evans M.E., Heller F. Environmental Magnetism: Principles and Applications of Enviromagnetics. San Diego, Acad. Press, 2003. 311 p.
6. Liu Q., Robersts A.P., Larrasoaña J.C., Banerjee S.K., Guyodo Y., Tauxe L., Oldfield F. Environmental magnetism: Principles and applications. *Rev. Geophys*., 2012, vol. 50, no. 4, Art. RG4002, pp. 1–50. doi: 10.1029/2012RG000393.
7. Preisach F. Über die magnetische Nachwirkung. *Zeitschrift Phys*., 1935, vol. 94, no. 5–6, pp. 277–302.
8. Mayergoyz I.D. Mathematical models of hysteresis. *Phys. Rev. Lett*., 1986, vol. 56, pp. 1518–1521.
9. Hejda P., Zelinka T. Modeling of hysteresis processes in magnetic rock samples using the Preisach diagram. *Phys. Earth Planet. Inter*., 1990, vol. 63, no. 1–2, pp. 32–40.
10. Fabian K., von Dobeneck T. Isothermal magnetization of samples with stable Preisach function: A survey of hysteresis, remanence, and rock magnetic parameters. *J. Geophys. Res*., 1997, vol. 102, no. B8, pp. 17659–17677.
11. Newell A.J. A high-precision model of first-order reversal curve (FORC) functions for single-domain ferromagnets with uniaxial anisotropy. *Geochem. Geophys. Geosys*., 2005, vol. 6, no. 5, Art. Q05010, pp. 1–14. doi: 10.1029/2004GC000877.
12. Egli R., Chen A.P., Winklhofer M., Kodama K.P., Horng C.-S. Detection of noninteracting single domain particles using first-order reversal curve diagrams. *Geochem. Geophys. Geosys*., 2010, vol. 11, no. 1, Art. Q01Z11, pp. 1–22. doi: 10.1029/2009GC002916.
13. Woodward J.G., Della Torre E. Particle interaction in magnetic recording tapes. *J. Appl. Phys*., 1960, vol. 31, no. 1, pp. 56–62.
14. Basso V., Bertotti G. Description of magnetic interactions and Henkel plots by the Preisach hysteresis model. *IEEE Trans. Magn*., 1994, vol. 30, no. 1, pp. 64–72.
15. Pike C.R., Roberts A.P., Verosub K.L. Characterizing interactions in fine magnetic particle systems using first order reversal curves. *J. Appl. Phys*., 1999, vol. 85, no. 9, pp. 6660–6667.
16. Muxworthy A.R., Williams W. Magnetostatic interaction fields in first-order-reversal curve diagrams. *J. Appl. Phys*., 2005, vol. 97, no. 6, Art. 063905, pp. 1–5.
17. Egli R. Theoretical aspects of dipolar interactions and their appearance in first-order reversal curves of thermally activated single-domain particles. *J. Geophys. Res*., 2006, vol. 111, no. B12, Art. B12S17, pp. 1–18. doi: 10.1029/2006JB004567.
18. Muxworthy A.R., Dunlop D.J. First-order reversal curve (FORC) diagrams for pseudo-single-domain magnetites at high temperature. *Earth Planet. Sci. Lett*., 2002, vol. 203, no. 1, pp. 369–382.
19. Carvallo C., Muxworthy A.R., Dunlop D.J., Williams W. Micromagnetic modeling of first-order reversal curve (FORC) diagrams for single-domain and pseudo-single-domain magnetite. *Earth Planet. Sci. Lett*., 2003, vol. 213, no. 3–4, pp. 375–390.

20. Winklhofer M., Dumas R.K., Liu K. Identifying reversible and irreversible magnetization changes in prototype patterned media using first- and second-order reversal curves. *J. Appl. Phys*., 2008, vol. 103, no. 7, Art. 07C518, pp. 1–3.
21. Pike C.R., Roberts A.P., Dekkers M.J., Verosub K.L. An investigation of multi-domain hysteresis mechanism using FORC diagrams. *Phys. Earth Planet. Inter*., 2001, vol. 126, no. 1–2, pp. 11–25.
22. Church N., Feinberg J.M., Harrison R. Low-temperature domain wall pinning in titanomagnetite: Quantitative modeling of multidomain first-order reversal curve diagrams and AC susceptibility. *Geochem. Geophys. Geosys*., 2011, vol. 12, no. 7, Art. Q07Z27, pp. 1–18. doi: 10.1029/GC003538.
23. Katzgraber H.G., Pázmándi F., Pike C.R., Liu K., Scalettar R.T., Verosub K.L., Zimányi G.T. Reversal-field memory in the hysteresis of spin glasses. *Phys. Rev. Lett*., 2002, vol. 89, no. 25, Art. 257202, pp. 1–4.
24. Roberts A.P., Pike C.R., Verosub K.L. First-order reversal curve diagrams: A new tool for characterizing the magnetic properties of natural samples. *J. Geophys. Res*., 2000, vol. 105, no. B12, pp. 28461–28475.
25. Roberts A.P., Liu Q., Rowan C.J., Chang L., Carvallo C., Torrent J., Horng C.-H. Characterization of hematite (α-Fe_2O_3), goethite (α-FeOOH), greigite (Fe_3S_4), and pyrrhotite (Fe_7S_8) using first-order reversal curve diagrams. *J. Geophys. Res*., 2006, vol. 111, no. B12, Art. B12S35, pp. 1–16. doi: 10.1029/2006JB004715.
26. Roberts A.P., Chang L., Heslop D., Florindo F., Larrasoaña J.C. Searching for single domain magnetite in the 'pseudo-single-domain' sedimentary haystack: Implications of biogenic magnetite preservation for sediment magnetism and relative paleointensity determinations. *J. Geophys. Res*., 2012, vol. 117, no. B8, Art. B08104, pp. 1–26. doi: 10.1029/2012JB 009412.
27. Roberts A.P., Florindo F., Villa G., Chang L., Jovine L., Bohaty S.M., Larrasoaña J.C., Heslop D., Fitz Gerald J.D. Magnetotactic bacterial abundance in pelagic marine environments is limited by organic carbon flux and availability of dissolved iron. *Earth Planet. Sci. Lett*., 2011, vol. 310, no. 3–4, pp. 441–452.
28. Yamazaki T., Ikehara M. Origin of magnetic mineral concentration variation in the Southern Ocean. *Paleoceanography*, 2012, vol. 27, no. 3, Art. PA2206, P. 1. doi: 10.1029/2011PA002271.
29. Egli R. VARIFORC: An optimized protocol for calculating non-regular first-order reversal curve (FORC) diagrams. *Global Planet. Change*, 2013, vol. 110, Pt. C, pp. 302–320. doi: 10.1016/j.gloplacha.2013.08.003.
30. Ludwig P., Egli R., Bishop S., Chernenko V., Frederichs T., Rugel G., Merchel S. Characterization of primary and secondary magnetite in marine sediment by combining chemical and magnetic unmixing techniques. *Global Planet. Change*, 2013, vol. 110, Pt. C, pp. 321–339. doi: 10.1016/j.gloplacha.2013.08.018.
31. Winklhofer M., Zimanyi G.T. Extracting the intrinsic switching field distribution in perpendicular media: A comparative analysis. *J. Appl. Phys*., 2006, vol. 99, no. 8, Art. 08E710, pp. 1–3.
32. Pike C.R., Roberts A.P., Verosub K.L. First-order reversal curve diagrams and thermal relaxation effects in magnetic particles. *Geophys. J. Int*., 2001, vol. 145, no. 3, pp. 721–730.
33. Heslop D., Muxworthy A. Aspects of calculating first-order reversal curve distributions. *J. Mag. Magn. Mat*., 2005, vol. 288, pp. 155–167.
34. Harrison R.J., Feinberg J.M. FORCinel: An improved algorithm for calculating first-order reversal curve distributions using locally weighted regression smoothing. *Geochem. Geophys. Geosys*., 2008, vol. 9, no. 5, Art. Q05016, pp. 1–11. doi: 10.1029/2008GC001987.

35. Heslop D., Roberts A.P. Estimation of significance levels and confidence intervals for first-order reversal curve distributions. *Geochem. Geophys. Geosys*., 2012, vol. 13, no. 5, Art. Q12Z40, pp. 1–12. doi: 10.1029/2012GC004115.
36. Ewing J.A. Experimental researches in magnetism. *Phil. Trans. R. Soc. Lond. A*, 1885, vol. 176, pp. 523–640.
37. Day R., Fuller M., Schmidt V.A. Hysteresis properties of titanomagnetites: Grain size and composition dependence. *Phys. Earth Planet. Inter*., 1977, vol. 13, no. 4, pp. 260–267.
38. Dunlop D.J. Theory and application of the Day plot (M_{rs}/M_s versus H_{cr}/H_c). 1. Theoretical curves and tests using titanomagnetite data. *J. Geophys. Res*., 2002, vol. 107, no. B3, Art. EPM 4, pp. 1–22. doi: 10.1029/2001JB 000486.
39. Dunlop D.J. Theory and application of the Day plot (M_{rs}/M_s versus H_{cr}/H_c). 2. Application to data for rocks, sediments, and soils. *J. Geophys. Res*., 2002, vol. 107, no. B3, Art. EPM 5, pp. 1–15. doi: 10.1029/ 2001JB 000487.
40. Néel L. Sur les effets d'un couplage entre grains ferromagnétiques doues d'hysteresis. *C.R. Acad. Sci*., 1958, vol. 246, pp. 2313–2319.
41. Stoner E.C., Wohlfarth E.P. A mechanism of magnetic hysteresis in heterogeneous alloys. *Phil. Trans. R. Soc. Lond. A*, 1948, vol. 240, pp. 599–642.
42. Pike C.R. First-order reversal-curve diagrams and reversible magnetization. *Phys. Rev. B*, 2003, vol. 68, Art. 104424, pp. 1–5.
43. Carvallo C., Dunlop D.J., Özdemir Ö. Experimental comparison of FORC and remanent Preisach diagrams. *Geophys. J. Int*., 2005, vol. 162, no. 3, pp. 747–754.
44. Vajda F., Della Torre E. Measurements of output-dependent Preisach functions. *IEEE Trans. Magn*., 1991, vol. 27, no. 6, pp. 4757–4762.
45. Mitchler P.D., Dan Dahlberg E., Wesseling E.E., Roshko R.M. Henkel plots in a temperature and time dependent Preisach model. *IEEE Trans. Magn*., 1996, vol. 32, no. 4, pp. 3185–3194.
46. Borcia I.D., Spinu L., Stancu A. A Preisach-Néel model with thermally variable variance. *IEEE Trans. Magn*., 2002, vol. 38, no. 5, pp. 2415–2417.
47. Winklhofer M., Dumas R.K., Liu K. Identifying reversible and irreversible magnetization changes in prototype patterned media using first- and second-order reversal curves. *J. Appl. Phys*., 2008, vol. 103, no. 7, Art. 07C518, pp. 1–3. doi: 10.1063/1.2837888.
48. Shcherbakov V.P., Winklhofer M., Hanzlik M., Petersen N. Elastic stability of chains of magnetosomes in magnetotactic bacteria. *Eur. Biophys. J*., 1997, vol. 26, no. 4, pp. 319–326.
49. Fabian K. Some additional parameters to estimate domain state from isothermal magnetization measurements. *Earth Planet. Sci. Lett*., 2003, vol. 213, no. 3–4, pp. 337–345.
50. Wohlfarth E.P. Relations between different modes of acquisition of the remanent magnetization of ferromagnetic particles. *J. Appl. Phys*., 1958, vol. 29, no. 3, pp. 595–596.
51. Muxworthy A., Williams W., Virdee D. Effect of magnetostatic interactions on the hysteresis parameters of single-domain and pseudo-single-domain grains. *J. Geophys. Res*., 2003, vol. 108, no. B11, Art. 2517, pp. 1–13. doi: 10.1029/2003JB002588.
52. Li J., Wu W., Liu Q., Pan Y. Magnetic anisotropy, magnetostatic interactions, and identification of magnetofossils. *Geochem. Geophys. Geosys*., 2012, vol. 13, no. 12, Art. Q10Z51, pp. 1–16. doi: 10.1029/2012GC004384.
53. Kopp R.E., Raub T.D., Schumann D., Vali H., Smirnov A.V., Kirschvink J.L. Magnetofossil spike during the Paleocene-Eocene thermal maximum: Ferromagnetic resonance, rock magnetic, and electron microscopy evidence from Ancora, New Jersey, United States. *Paleoceanograpy*, 2007, vol. 22, no. 4, Art. PA4103, pp. 1–7. doi: 10.1029/2007PA001473.

54. Lippert P.C., Zachos J.C. A biogenic origin for anomalous fine-grained magnetic material at the Paleocene-Eocene boundary at Wilson Lake, New Jersey. *Paleoceanography*, 2007, vol. 22, no. 4, Art. PA4104, pp. 1–8. doi: 10.1029/2007PA001471.

55. Wang H., Kent D.V., Jackson M.J. Evidence for abundant isolated magnetic nanoparticles at the Paleocene–Eocene boundary. *Proc. Natl. Acad. Sci. USA*, 2013, vol. 110, no. 2, pp. 425–430. doi: 10.1073/pnas.1205308110.

56. Sparks N.H.C., Mann S., Bazylinski D.A., Lovley D.R., Jannash H.W., Frankel R.B. Structure and morphology of magnetite anaerobically-produced by a marine magnetotactic bacterium and a dissimilatory iron-reducing bacterium. *Earth Planet. Sci. Lett*., 1990, vol. 98, no. 1, pp. 14–22.

57. Jacobs I.S., Bean C.P. An approach to elongated fine-particle magnets. *Phys. Rev*., 1955, vol. 100, no. 4, pp. 1060–1067.

58. Kobayashi A., Krischvink J.L., Nash C.Z., Kopp R.E., Sauer D.A., Bertani L.E., Voorhout W.F., Taguchi T. Experimental observation of magnetosome chain collapse in magnetotactic bacteria: Sedimentological, paleomagnetic, and evolutionary implications. *Earth Planet. Sci. Lett*., 2006, vol. 245, no. 3–4, pp. 538–550.

59. Tauxe L., Steindorf J.L., Harris A. Depositional remanent magnetization: Toward an improved theoretical and experimental foundation. *Earth Planet. Sci. Lett*., 2006, vol. 244, no. 3–4, pp. 515–529.

60. Chen A.P., Egli R., Moskowitz B.M. First-order reversal curve (FORC) of natural and cultured biogenic magnetite. *J. Geophys. Res*., 2007, vol. 112, Art. B08S90, pp. 1–13. doi: 10.1029/2006JB 004575.

61. Newell A.J., Merrill R.T. Nucleation and stability of ferromagnetic states. *J. Geophys. Res*., 2000, vol. 105, no. B8, pp. 19377–19391.

62. Dumas R.K., Li C.-P., Roshchin I.V., Schuller I.K., Liu K. Magnetic fingerprints of sub-100 nm Fe dots. *Phys. Rev. B*, 2007, vol. 75, Art. 134405, pp. 1–5.

63. Lappe S.-C., Church N.S., Kasama T., Bastos da Silva Fanta A., Bromiley G., Dunin-Borkowski R.E., Feinberg J.M., Russell S., Harrison R.J. Mineral magnetism of dusty olivine: A credible recorder of pre-accretionary remanence. *Geochem. Geophys. Geosys*., 2011, vol. 12, no. 12, Art. Q12Z35, pp. 1–20. doi: 10.1029/2011GC003811.

64. Wehland F., Leonhardt R., Vadeboin F., Appel E. Magnetic interaction analysis of basaltic samples and pre-selection for absolute paleointensity measurements. *Geophys. J. Int*., 2005, vol. 162, no. 2, pp. 315–320. doi: 10.1111/j.1365-246X.2005.02429.x

65. Carvallo C., Roberts A.P., Leonhardt R., Laj C., Kissel C., Perrin M., Camps P. Increasing the efficiency of paleointensity analyses by selection of samples using first-order reversal curve diagrams. *J. Geophys. Res*., 2006, vol. 111, no. B12, Art. B12103, pp. 1–15. doi: 10.1029/2005JB 004126.

66. Acton G., Yin Q.-Z., Verosub K.L., Jovane L., Roth A., Jacobsen B., Ebel D.S. Micromagnetic coercivity distributions and interactions in chondrules with implications for paleointensities of the early solar system. *J. Geophys. Res*., 2007, vol. 112, no. B3, Art. B03S90, pp. 1–19. doi: 10.1029/2006JB 004655.

67. Muxworthy A.R., Heslop D. A Preisach method for estimating absolute paleofield intensity under the constraint of using only isothermal measurements: 1. Theoretical framework. *J. Geophys. Res*., 2011, vol. 116, no. B4, Art. B04102, pp. 1–13. doi: 10.1029/2010JB007843.

68. Muxworthy A.R., Heslop D., Paterson G.A., Michalk D. A Preisach method for estimating absolute paleofield intensity under the constraint of using only isothermal measurements: 2. Experimental testing. *J. Geophys. Res*., 2011, vol. 116, no. B4, Art. B04103, pp. 1–20. doi: 10.1029/2010 JB007844.

69. Dunlop D.J., Wescott-Lewis M.F., Bailey M.E. Preisach diagrams and anhysteresis: do they measure interactions? *Phys. Earth Planet. Inter*., 1990, vol. 65, no. 1–2, pp. 62–77.

70. Kind K., Gehring A.U., Winklhofer M., Hirt A.M. Combined use of magnetometry and spectroscopy for identifying magnetofossils in sediments. *Geochem. Geophys. Geosys*., 2011, vol. 12, no. 8, Art. Q08008, pp. 1–13. doi: 10.1029/2011GC003633.

Received
December 27, 2013

Egli, Ramon – PhD, Head of Geomagnetism and Gravimetry Department, Central Institute for Meteorology and Geodynamics, Vienna, Austria.
E-mail: *r.egli@zamg.ac.at*

Winklhofer, Michael – PhD, Adjunct Professor, Department for Earth and Environmental Sciences, Ludwig Maximilian University of Munich, Munich, Germany.
E-mail: *michael@geophysik.uni-muenchen.de*

* * *

ПОСЛЕДНИЕ ДОСТИЖЕНИЯ В ОБЛАСТИ ОБРАБОТКИ И ИНТЕРПРЕТАЦИИ КРИВЫХ ПЕРЕМАГНИЧИВАНИЯ ПЕРВОГО ПОРЯДКА (КППП)

Р. Эгли, М. Винкльхофер

Аннотация

Недавние достижения в области палеомагнетизма и магнетизма окружающей среды основаны на измерениях кривых перемагничивания первого порядка (КППП). К наиболее значимым примерам относятся обнаружение ископаемых магнетосом, производимых магнетотактическими бактериями, а также определение абсолютной палеонапряженности термочувствительных образцов, таких как метеориты. В основе дальнейшего развития этих научных направлений лежит более детальное изучение естественных магнитных минеральных комплексов. Перспективы таких исследований видятся в разработке, с одной стороны, протоколов обработки КППП, а с другой – моделей для идеализированных магнитных систем. До сих пор диаграммы КППП использовались главным образом как инструмент для качественной индикации доменных состояний магнитных частиц при отсутствии количественных связей с другими магнитными параметрами. Данная работа связывает основные характеристики КППП со стандартными гистерезисными параметрами на основе используемых в методе КППП трех типов намагниченности и соответствующих распределений коэрцитивности. Одним из таких параметров является остаточная намагниченность насыщения, размагничивание которой по методике КППП в нулевом постоянном поле даёт возможность получить распределение коэрцитивной силы образца. Другие два типа намагниченности связаны с необратимыми процессами, происходящими в ходе получения петель гистерезиса, и инверсионной симметрией магнитных состояний изолированных частиц. В совокупности эти намагниченности дают исчерпывающую информацию о процессах намагничивания в однодоменных, псевдооднодоменных и многодоменных частицах. В отличие от параметров гистерезиса, используемых в так называемой диаграмме Дея, эти намагниченности не подвержены воздействию обратимых процессов (например, суперпарамагнетизма) и поэтому хорошо подходят для надежного определения доменного состояния носителей остаточной намагниченности. Пакет программного обеспечения VARIFORC был разработан с целью проведения детальных исследований КППП и расчета описанных выше трех типов распределений коэрцитивности. Основные примеры таких расчетов представлены в статье и доступны для скачивания вместе с пакетом VARIFORC.

Ключевые слова: магнетизм горных пород, палеомагнетизм, магнетизм окружающей среды, характеристика магнитных минералов, магнитный гистерезис, кривые перемагничивания первого порядка, магнитные окаменелости, состояния магнитного домена.

Литература

1. *Chikazumi S.* Physics of Ferromagnetism. – N. Y.: Oxford Univ. Press, 1997. – 682 p.
2. *Coey J.M.D.* Magnetism and Magnetic Materials. – Cambridge: Cambridge Univ. Press, 2010. – 625 p.
3. *Dunlop D.J., Özdemir Ö.* Rock Magnetism: Fundamentals and Frontiers. – Cambridge: Cambridge Univ. Press, 1997. – 594 p.
4. *Tauxe L.* Essentials of Paleomagnetism. – Berkeley: University of California Press, 2010. – 505 p.
5. *Evans M.E., Heller F.* Environmental Magnetism: Principles and Applications of Enviromagnetics. – San Diego: Acad. Press, 2003. – 311 p.
6. *Liu Q., Robersts A.P., Larrasoaña J.C., Banerjee S.K., Guyodo Y., Tauxe L., Oldfield F.* Environmental magnetism: Principles and applications // Rev. Geophys. – 2012. – V. 50, No 4. – Art. RG4002, P. 1–50. – doi: 10.1029/2012RG000393.
7. *Preisach F.* Über die magnetische Nachwirkung // Zeitschrift Phys. – 1935. – V. 94, No 5–6. – P. 277–302.
8. *Mayergoyz I.D.* Mathematical models of hysteresis // Phys. Rev. Lett. – 1986. – V. 56. – P. 1518–1521.
9. *Hejda P., Zelinka T.* Modeling of hysteresis processes in magnetic rock samples using the Preisach diagram // Phys. Earth Planet. Inter. – 1990. – V. 63, No 1–2. – P. 32–40.
10. *Fabian K., von Dobeneck T.* Isothermal magnetization of samples with stable Preisach function: A survey of hysteresis, remanence, and rock magnetic parameters // J. Geophys. Res. – 1997. – V. 102, No B8. – P. 17659–17677.
11. *Newell A.J.* A high-precision model of first-order reversal curve (FORC) functions for single-domain ferromagnets with uniaxial anisotropy // Geochem. Geophys. Geosys. – 2005. – V. 6, No 5. – Art. Q05010, P. 1–14. – doi: 10.1029/2004GC000877.
12. *Egli R., Chen A.P., Winklhofer M., Kodama K.P., Horng C.-S.* Detection of noninteracting single domain particles using first-order reversal curve diagrams // Geochem. Geophys. Geosys. – 2010. – V. 11, No 1. – Art. Q01Z11, P. 1–22. – doi: 10.1029/2009GC002916.
13. *Woodward J.G., Della Torre E.* Particle interaction in magnetic recording tapes // J. Appl. Phys. – 1960. – V. 31, No 1. – P. 56–62.
14. *Basso V., Bertotti G.* Description of magnetic interactions and Henkel plots by the Preisach hysteresis model // IEEE Trans. Magn. – 1994. – V. 30, No 1. – P. 64–72.
15. *Pike C.R., Roberts A.P., Verosub K.L.* Characterizing interactions in fine magnetic particle systems using first order reversal curves // J. Appl. Phys. – 1999. – V. 85, No 9. – P. 6660–6667.
16. *Muxworthy A.R., Williams W.* Magnetostatic interaction fields in first-order-reversal curve diagrams // J. Appl. Phys. – 2005. – V. 97, No 6. – P. 063905-1–063905-5.
17. *Egli R.* Theoretical aspects of dipolar interactions and their appearance in first-order reversal curves of thermally activated single-domain particles // J. Geophys. Res. – 2006. – V. 111, No B12. – Art. B12S17, P. 1–18. – doi: 10.1029/2006JB004567.
18. *Muxworthy A.R., Dunlop D.J.* First-order reversal curve (FORC) diagrams for pseudo-single-domain magnetites at high temperature // Earth Planet. Sci. Lett. – 2002. – V. 203, No 1. – P. 369–382.
19. *Carvallo C., Muxworthy A.R., Dunlop D.J., Williams W.* Micromagnetic modeling of first-order reversal curve (FORC) diagrams for single-domain and pseudo-single-domain magnetite // Earth Planet. Sci. Lett. – 2003. – V. 213, No 3–4. – P. 375–390.
20. *Winklhofer M., Dumas R.K., Liu K.* Identifying reversible and irreversible magnetization changes in prototype patterned media using first- and second-order reversal curves // J. Appl. Phys. – 2008. – V. 103, No 7. – P. 07C518-1–07C518-3.
21. *Pike C.R., Roberts A.P., Dekkers M.J., Verosub K.L.* An investigation of multi-domain hysteresis mechanism using FORC diagrams // Phys. Earth Planet. Inter. – 2001. – V. 126, No 1–2. – P. 11–25.
22. *Church N., Feinberg J.M., Harrison R.* Low-temperature domain wall pinning in titanomagnetite: Quantitative modeling of multidomain first-order reversal curve diagrams and AC susceptibility // Geochem. Geophys. Geosys. – 2011. – V. 12, No 7. – Art. Q07Z27, P. 1–18. – doi: 10.1029/GC003538.

23. *Katzgraber H.G., Pázmándi F., Pike C.R., Liu K., Scalettar R.T., Verosub K.L., Zimányi G.T.* Reversal-field memory in the hysteresis of spin glasses // Phys. Rev. Lett. – 2002. – V. 89, No 25. – P. 257202-1–257202-4.
24. *Roberts A.P., Pike C.R., Verosub K.L.* First-order reversal curve diagrams: A new tool for characterizing the magnetic properties of natural samples // J. Geophys. Res. – 2000. – V. 105, No B12. – P. 28461–28475.
25. *Roberts A.P., Liu Q., Rowan C.J., Chang L., Carvallo C., Torrent J., Horng C.-H.* Characterization of hematite (α-Fe_2O_3), goethite (α-FeOOH), greigite (Fe_3S_4), and pyrrhotite (Fe_7S_8) using first-order reversal curve diagrams // J. Geophys. Res. – 2006. – V. 111, No B12. – Art. B12S35, P. 1–16. – doi: 10.1029/2006JB004715.
26. *Roberts A.P., Chang L., Heslop D., Florindo F., Larrasoaña J.C.* Searching for single domain magnetite in the 'pseudo-single-domain' sedimentary haystack: Implications of biogenic magnetite preservation for sediment magnetism and relative paleointensity determinations // J. Geophys. Res. – 2012. – V. 117, No B8. – Art. B08104, P. 1–26. – doi: 10.1029/2012JB 009412.
27. *Roberts A.P., Florindo F., Villa G., Chang L., Jovine L., Bohaty S.M., Larrasoaña J.C., Heslop D., Fitz Gerald J.D.* Magnetotactic bacterial abundance in pelagic marine environments is limited by organic carbon flux and availability of dissolved iron // Earth Planet. Sci. Lett. – 2011. – V. 310, No 3–4. – P. 441–452.
28. *Yamazaki T., Ikehara M.* Origin of magnetic mineral concentration variation in the Southern Ocean // Paleoceanography. – 2012. – V. 27, No 3. – Art. PA2206, P. 1. – doi: 10.1029/2011PA002271.
29. *Egli R.* VARIFORC: An optimized protocol for calculating non-regular first-order reversal curve (FORC) diagrams // Global Planet. Change. – 2013. – V. 110, Pt. C. – P. 302–320. – doi: 10.1016/j.gloplacha.2013.08.003.
30. *Ludwig P., Egli R., Bishop S., Chernenko V., Frederichs T., Rugel G., Merchel S.* Characterization of primary and secondary magnetite in marine sediment by combining chemical and magnetic unmixing techniques // Global Planet. Change. – 2013. – V. 110, Pt. C. – P. 321–339. – doi: 10.1016/j.gloplacha.2013.08.018.
31. *Winklhofer M., Zimanyi G.T.* Extracting the intrinsic switching field distribution in perpendicular media: A comparative analysis // J. Appl. Phys. – 2006. – V. 99, No 8. – P. 08E710-1–08E710-3.
32. *Pike C.R., Roberts A.P., Verosub K.L.* First-order reversal curve diagrams and thermal relaxation effects in magnetic particles // Geophys. J. Int. – 2001. – V. 145, No 3. – P. 721–730.
33. *Heslop D., Muxworthy A.* Aspects of calculating first-order reversal curve distributions // J. Mag. Magn. Mat. – 2005. – V. 288. – P. 155–167.
34. *Harrison R.J., Feinberg J.M.* FORCinel: An improved algorithm for calculating first-order reversal curve distributions using locally weighted regression smoothing // Geochem. Geophys. Geosys. – 2008. – V. 9, No. 5. – Art. Q05016, P. 1–11. – doi: 10.1029/2008GC001987.
35. *Heslop D., Roberts A.P.* Estimation of significance levels and confidence intervals for first-order reversal curve distributions // Geochem. Geophys. Geosys. – 2012. – V. 13, No 5. – Art. Q12Z40, P. 1–12. – doi: 10.1029/2012GC004115.
36. *Ewing J.A.* Experimental researches in magnetism // Phil. Trans. R. Soc. Lond. A. – 1885. – V. 176. – P. 523–640.
37. *Day R., Fuller M., Schmidt V.A.* Hysteresis properties of titanomagnetites: Grain size and composition dependence // Phys. Earth Planet. Inter. – 1977. – V. 13, No 4. – P. 260–267.
38. *Dunlop D.J.* Theory and application of the Day plot (M_{rs}/M_s versus H_{cr}/H_c). 1. Theoretical curves and tests using titanomagnetite data // J. Geophys. Res. – 2002. – V. 107, No B3. – P. EPM 4-1–EPM 4-22. – doi: 10.1029/2001JB 000486.
39. *Dunlop D.J.* Theory and application of the Day plot (M_{rs}/M_s versus H_{cr}/H_c). 2. Application to data for rocks, sediments, and soils // J. Geophys. Res. – 2002. – V. 107, No B3. – P. EPM 5-1–EPM 5-15. – doi: 10.1029/2001JB 000487.
40. *Néel L.* Sur les effets d'un couplage entre grains ferromagnétiques doues d'hysteresis // C.R. Acad. Sci. – 1958. – V. 246. – P. 2313–2319.
41. *Stoner E.C., Wohlfarth E.P.* A mechanism of magnetic hysteresis in heterogeneous alloys // Phil. Trans. R. Soc. Lond. A. – 1948. – V. 240. – P. 599–642.

42. *Pike C.R.* First-order reversal-curve diagrams and reversible magnetization // Phys. Rev. B. – 2003. – V. 68. – P. 104424-1–104424-5.

43. *Carvallo C., Dunlop D.J., Özdemir Ö.* Experimental comparison of FORC and remanent Preisach diagrams // Geophys. J. Int. – 2005. – V. 162, No 3. – P. 747–754.

44. *Vajda F., Della Torre E.* Measurements of output-dependent Preisach functions // IEEE Trans. Magn. – 1991. – V. 27, No 6. – P. 4757–4762.

45. *Mitchler P.D., Dan Dahlberg E., Wesseling E.E., Roshko R.M.* Henkel plots in a temperature and time dependent Preisach model // IEEE Trans. Magn. – 1996. – V. 32, No 4. – P. 3185–3194.

46. *Borcia I.D., Spinu L., Stancu A.* A Preisach-Néel model with thermally variable variance // IEEE Trans. Magn. – 2002. – V. 38, No 5. – P. 2415–2417.

47. *Winklhofer M., Dumas R.K., Liu K.* Identifying reversible and irreversible magnetization changes in prototype patterned media using first- and second-order reversal curves // J. Appl. Phys. – 2008. – V. 103, No 7. – P. 07C518-1–07C518-3. – doi: 10.1063/1.2837888.

48. *Shcherbakov V.P., Winklhofer M., Hanzlik M., Petersen N.* Elastic stability of chains of magnetosomes in magnetotactic bacteria // Eur. Biophys. J. – 1997. – V. 26, No 4. – P. 319–326.

49. *Fabian K.* Some additional parameters to estimate domain state from isothermal magnetization measurements // Earth Planet. Sci. Lett. – 2003. – V. 213, No 3–4. – P. 337–345.

50. *Wohlfarth E.P.* Relations between different modes of acquisition of the remanent magnetization of ferromagnetic particles // J. Appl. Phys. – 1958. – V. 29, No 3. – P. 595–596.

51. *Muxworthy A., Williams W., Virdee D.* Effect of magnetostatic interactions on the hysteresis parameters of single-domain and pseudo-single-domain grains // J. Geophys. Res. – 2003. – V. 108, No B11. – Art. 2517, P. 1–13. – doi: 10.1029/2003JB002588.

52. *Li J., Wu W., Liu Q., Pan Y.* Magnetic anisotropy, magnetostatic interactions, and identification of magnetofossils // Geochem. Geophys. Geosys. – 2012. – V. 13, No 12. – Art. Q10Z51, P. 1–16. – doi: 10.1029/2012GC004384.

53. *Kopp R.E., Raub T.D., Schumann D., Vali H., Smirnov A.V., Kirschvink J.L.* Magnetofossil spike during the Paleocene-Eocene thermal maximum: Ferromagnetic resonance, rock magnetic, and electron microscopy evidence from Ancora, New Jersey, United States // Paleoceanograpy. – 2007. – V. 22, No 4. – Art. PA4103, P. 1–7. – doi: 10.1029/2007PA001473.

54. *Lippert P.C., Zachos J.C.* A biogenic origin for anomalous fine-grained magnetic material at the Paleocene-Eocene boundary at Wilson Lake, New Jersey // Paleoceanography. – 2007. – V. 22, No 4. – Art. PA4104, P. 1–8. – doi: 10.1029/2007PA001471.

55. *Wang H., Kent D.V., Jackson M.J.* Evidence for abundant isolated magnetic nanoparticles at the Paleocene–Eocene boundary // Proc. Natl. Acad. Sci. USA. – 2013. – V. 110, No 2. – P. 425–430. – doi: 10.1073/pnas.1205308110.

56. *Sparks N.H.C., Mann S., Bazylinski D.A., Lovley D.R., Jannash H.W., Frankel R.B.* Structure and morphology of magnetite anaerobically-produced by a marine magnetotactic bacterium and a dissimilatory iron-reducing bacterium // Earth Planet. Sci. Lett. – 1990. – V. 98, No 1. – P. 14–22.

57. *Jacobs I.S., Bean C.P.* An approach to elongated fine-particle magnets // Phys. Rev. – 1955. – V. 100, No 4. – P. 1060–1067.

58. *Kobayashi A., Krischvink J.L., Nash C.Z., Kopp R.E., Sauer D.A., Bertani L.E., Voorhout W.F., Taguchi T.* Experimental observation of magnetosome chain collapse in magnetotactic bacteria: Sedimentological, paleomagnetic, and evolutionary implications // Earth Planet. Sci. Lett. – 2006. – V. 245, No 3–4. – P. 538–550.

59. *Tauxe L., Steindorf J.L., Harris A.* Depositional remanent magnetization: Toward an improved theoretical and experimental foundation // Earth Planet. Sci. Lett. – 2006. – V. 244, No 3–4. – P. 515–529.

60. *Chen A.P., Egli R., Moskowitz B.M.* First-order reversal curve (FORC) of natural and cultured biogenic magnetite // J. Geophys. Res. – 2007. – V. 112. – Art. B08S90, P. 1–13. – doi: 10.1029/2006JB004575.

61. *Newell A.J., Merrill R.T.* Nucleation and stability of ferromagnetic states // J. Geophys. Res. – 2000. – V. 105, No B8. – P. 19377–19391.

62. *Dumas R.K., Li C.-P., Roshchin I.V., Schuller I.K., Liu K.* Magnetic fingerprints of sub-100 nm Fe dots // Phys. Rev. B. – 2007. – V. 75. – P. 134405-1–134405-5.

63. *Lappe S.-C., Church N.S., Kasama T., Bastos da Silva Fanta A., Bromiley G., Dunin-Borkowski R.E., Feinberg J.M., Russell S., Harrison R.J.* Mineral magnetism of dusty olivine: A credible recorder of pre-accretionary remanence // Geochem. Geophys. Geosys. – 2011. – V. 12, No 12. – Art. Q12Z35, P. 1–20. – doi: 10.1029/2011GC003811.

64. *Wehland F., Leonhardt R., Vadeboin F., Appel E.* Magnetic interaction analysis of basaltic samples and pre-selection for absolute paleointensity measurements // Geophys. J. Int. – 2005. – V. 162, No 2. – P. 315–320. – doi: 10.1111/j.1365-246X.2005.02429.x

65. *Carvallo C., Roberts A.P., Leonhardt R., Laj C., Kissel C., Perrin M., Camps P.* Increasing the efficiency of paleointensity analyses by selection of samples using first-order reversal curve diagrams // J. Geophys. Res. – 2006. – V. 111, No B12. – Art. B12103, P. 1–15. – doi: 10.1029/2005JB004126.

66. *Acton G., Yin Q.-Z., Verosub K.L., Jovane L., Roth A., Jacobsen B., Ebel D.S.* Micromagnetic coercivity distributions and interactions in chondrules with implications for paleointensities of the early solar system // J. Geophys. Res. – 2007. – V. 112, No B3. – Art. B03S90, P. 1–19. – doi: 10.1029/2006JB 004655.

67. *Muxworthy A.R., Heslop D.* A Preisach method for estimating absolute paleofield intensity under the constraint of using only isothermal measurements: 1. Theoretical framework // J. Geophys. Res. – 2011. – V. 116, No B4. – Art. B04102, P. 1–13. – doi: 10.1029/2010JB007843.

68. *Muxworthy A.R., Heslop D., Paterson G.A., Michalk D.* A Preisach method for estimating absolute paleofield intensity under the constraint of using only isothermal measurements: 2. Experimental testing // J. Geophys. Res. – 2011. – V. 116, No B4. – Art. B04103, P. 1–20. – doi: 10.1029/2010 JB007844.

69. *Dunlop D.J., Wescott-Lewis M.F., Bailey M.E.* Preisach diagrams and anhysteresis: do they measure interactions? // Phys. Earth Planet. Inter. – 1990. – V. 65, No 1–2. – P. 62–77.

70. *Kind K., Gehring A.U., Winklhofer M., Hirt A.M.* Combined use of magnetometry and spectroscopy for identifying magnetofossils in sediments // Geochem. Geophys. Geosys. – 2011. – V. 12, No 8. – Art. Q08008, P. 1–13. – doi: 10.1029/2011GC003633.

Поступила в редакцию
24.01.14

Эгли, Рамон – доктор наук, заведующий отделением геомагнетизма и гравиметрии, Центральный институт метеорологии и геодинамики, г. Вена, Австрия.
E-mail: *r.egli@zamg.ac.at*

Винкльхофер, Михаэль – доктор наук, адъюнкт-профессор кафедры наук о земле и окружающей среде, Мюнхенский университет Людвига-Максимилиана, г. Мюнхен, Германия.
E-mail: *michael@geophysik.uni-muenchen.de*